

Czech Technical University in Prague
Faculty of Nuclear Sciences and Physical Engineering

Obor: Fyzikální inženýrství
Zaměření: Fyzika a technika termojaderné fúze



**Development of diagnostics system
for plasma rotation measurement on
the tokamak COMPASS**

RESEARCH WORK

Autor: Bc. Tomáš Odstrčil
Supervisor: Ing. Diana Naydenková
Year: 2011

Název práce:

Vývoj diagnostického systému pro měření rotace plazmatu na tokamaku COMPASS

Autor: Bc. Tomáš Odstrčil

Obor: Fyzikální inženýrství

Druh práce: Výzkumná práce

Vedoucí práce: Ing. Diana Naydenková
ÚFP AV ČR v.v.i.

Konzultant: —

Zadání: Tokamak COMPASS, divertorové zařízení s H-módem a geometrií plazmatu podobnou tokamaku ITER, byl předán z anglického CCFE do Ústavu fyziky plazmatu AV ČR, v.v.i. v Praze. K uskutečnění cílů vědeckého programu tokamaku COMPASS zaměřeného na fyziku H-módu a zkoumání oblasti pedestalu, byl nově nainstalován spektrometr s vysokou disperzí pro měření Dopplerova posunu spektrálních čar uhlíku CIII (464.8 nm) s časovým rozlišením. Cílem práce je seznámit se s metodou určení rotace plazmatu pomocí měření Dopplerova posuvu spektrálních čar příměsí plazmatu, zprovoznění optické části měřícího systému a vyhodnocení rotace plazmatu z provedených měření.

Klíčová slova: Poloidální rychlost plazmatu, Dopplerův posuv, spektroskopie, tokamak, COMPASS

Title:

Development of diagnostics system for plasma rotation measurement on the tokamak COMPASS

Author: Bc. Tomáš Odstrčil

Key words: Poloidal plasma velocity, Doppler shift, spectroscopy, tokamak, COMPASS

Contents

Introduction	6
1 Experimental Setup	7
1.1 High Dispersion Spectrometer	7
1.2 Low Light Imaging Camera	8
1.3 Poloidal Observation System	10
1.3.1 Optical Path	10
1.3.2 The Radiant Flux Incoming to the Spectrometer	12
2 Signal Processing	13
2.1 Improving of SNR	13
2.1.1 Shot noise	13
2.1.2 Dark current	14
2.1.3 Readout Noise	14
2.1.4 Quantum Efficiency	15
2.1.5 Electron Multiplicative Noise	15
2.1.6 HXR noise	18
2.1.7 Background Light	18
2.1.8 SNR – Conclusion	18
2.2 Data Filtering	21
2.2.1 Median Filter	22
2.2.2 Low-pass Filter	22
2.2.3 A Priori Knowledge Base Filter	22
2.3 Model Function	22
3 Results and Discusion	27
3.1 Spectrometer	27

3.1.1	Dispersion	27
3.2	Instrumental Broadening	28
3.3	Plasma Rotation	29
3.4	Ion temperature	32
3.4.1	Line Integrated Temperature	32
3.4.2	Line Integrated Ion Temperature – Results	35
3.5	Asymmetrical Profile of the Spectral Lines	36
3.6	Intensities of the Observed Spectral Lines	38
3.6.1	Relative Intensities	38
3.6.2	Absolute Intensities	39
	Summary	42

Introduction

One of the goals of the actual fusion research is to increase energy confinement time. A great progress was done when the H-mode¹ was discovered [1] which almost doubled the energy confinement time. The exact understanding of the physics behind the H-mode is still incomplete. However, widely accepted theory is that the confinement time is increased because of suppression of the turbulent transport in plasma by rotation shear [2]. The majority source of momentum of plasma in large tokamaks is usually neutral beams, but also the spontaneous rotation is important, especially for ITER, where the power and momentum of NBIs will be insufficient.

The reason of the spontaneous (intrinsic) plasma rotation is still not completely explained. The neoclassical approach [3] significantly underestimate the intrinsic poloidal rotation of the plasma. Even more complex gyro-kinetics transport codes still are not able to predict exactly the real momentum transport coefficients. The current state of art is summarized in presentation [4]. The differences between the theoretical prediction and experimental results are presently studied on the most of the large tokamaks as JET, AUG, TCV, TEXTOR, ...

Those are the some of the reasons why the plasma rotation is also studied on tokamak COMPASS. The first experiments with plasma rotation were conducted during summer 2010, before installation of two NBI and results from these measurements are presented in this work. The newly installed NBI allows to measure influence of plasma by increased torque but also it will be possible to measure intrinsic rotation if the two NBI will be set in counter direction to suppress their torque.

The poloidal velocity of plasma edge is on tokamak COMPASS measured by Doppler shift of the CIII line. The high dispersion Portugal spectrometer [5] was used to measure the shift. Any other diagnostic that are able to measure the plasma rotation velocity are not currently presented in tokamak COMPASS, but in near future other spectrometer from IPP Garching will be installed and also a new CXRS² on the NBI will be installed. Also a reciprocal probe will be capable of measurement of the plasma rotation velocity in the SOL. Furthermore, after installation of the RC filters on power sources the more precise rotation of NTM modes will be measurable by magnetic diagnostics. The last but not least option is measure of the rotation and position of NTM instabilities by bolometer or SXR tomography.

¹High confinement mode

²Charge Exchange Recombination Spectroscopy

Chapter 1

Experimental Setup

In this chapter the properties of the used spectrometer, the camera and the optical path will be described. Also calculations of properties of the present optical path between plasma and spectrometer will be presented. The results are also applicable for the new planned optical path with installed beam splitter (Fig. 1.3).

1.1 High Dispersion Spectrometer

The high dispersion visible light spectrometer developed for ISTTOK tokamak in Portugal [5] has been designed for time resolved measurement of Doppler shift of the impurities lines. The spectrometer was designed for observation of narrow 20 \AA spectral region around 4650 \AA . It is the region where the CIII triplet occurs, one of the most intense impurities lines in visible spectrum of tokamak plasma radiation.

The spectrometer is based on a double monochromator in additive dispersion mode [6] made from two high density ruled concave diffraction gratings. This arrangement has been chosen because a higher efficiency for observed wavelength can be achieved compared to the spectrometer with one holographic grating with very high groove density. However, high throughput and higher dispersion was also achieved in the experiments with blazed gratings applied in high order [7].

The schema of the spectrometer is in Fig. 1.1, the light from tokamak is focused by collecting lens to the input variable width slit ($0\text{-}500 \mu\text{m} \times 20 \text{ mm}$). The light from slit incidence on the diffraction grating with 1 m radius of curvature and $60 \times 60 \text{ mm}^2$ area. The slit is situated on the Rowland circle of the first diffraction grating. The Rowland circle is a circle whose diameter is equal to radius of the concave grating, tangential to the surface of the grating and passes through grating centre [8]. For the input and output slit situated on the Rowland circle is guaranteed focus of the spectra in the plane perpendicular to the grating and the grooves, so called *dispersion plane*. The focus in the perpendicular plane, so called *sagittal plane*, is not generally ensured and therefore astigmatism of second and higher orders can be observed. This astigmatism was reduced by slightly non-equidistance grooves spacing [9, 5]. The astigmatism could be also suppressed by cylindrical lens of the appropriate focal length placed before the input slit.

Instead of the output slit used in the ordinary configuration of the monochromators, plane mirror positioned on the cross-section of the Rowland circle and *sagittal plane* of

the observed spectral line was used. The second grating should be set axially symmetrical to the first one, in the additive diffraction mode, so that the Rowland circle of its intersect the mirror at the same place as the circle of the first grating and also intersect output focal plane. Therefore, the incidence angle of the first should be equal to the diffraction angle of the second and also reversely.

The real configuration is more complicated and the photography with highlighted optical components is in Fig. 1.2. The Rowland circle of the second grating (green or red circle) cannot intersect the mirror and the output focal plane at the same time. Probably the focal plane of the first and the second grating do not lie on the mirror, but they are placed on the line between the mirror and the first grating.

The throughput of the whole device is $f/\# \approx 10$ and inverse linear dispersion is $1.7 \text{ \AA}/\text{mm}$. Other measured parameters of this spectrometer are in the Section 3.1.

1.2 Low Light Imaging Camera

The light from the spectrometer was collected by the high sensitive camera Andor DU-897E. The aim is to achieve high SNR¹ and also good time resolution. The highest achievable time resolution for full vertical binning is 0.5 ms. The A/D resolution is 14 bit for the 100 MHz readout speed, and 16 bit for the 1 MHz readout speed.

The resolution of CCD is 512×512 pixels and size of the pixel is $16 \times 16 \mu\text{m}^2$. The chip consist of two areas, the first is photosensitive for collecting of the light and the second is hidden and serves as a storage before readout. The camera supports on chip binding of the pixels and therefore signal quality and also the speed of camera can be significantly improved if full binning in vertical direction is used. The thermal noise of CCD is supressed by cooling down by Peltier element to -50°C . With installed water cooling can be achieved -100°C . The unique property of this CCD is built in electron multiplication (EM) amplifier. It is very useful for low light, high speed applications to suppress the influence of the readout noise. The principle of EM is similar to avalanche photodiodes, but at single ionization stage probability of creating of new electron is very low. Therefore, hundreds of the stages must be used. The problems, connected to this multiplication, are discussed in detail in Section 2.1.5.

The camera should be placed tangentially to the Rowland circle at the sagittal plane, where the observed spectral lines are focused (Fig. 1.1). However, from practical reasons the camera was placed parallel to the optical axis of the spectrometer. Consequences are decrease of the dispersion, increase of the light intensity and also increase of the instrumental broadening. Suppose that the angle between the tangential and used position is $\alpha \approx 30^\circ$. Then increase of the intensity connected with decrease of dispersion caused relative decrease of the precision of the observed Doppler shift of the lines to

$$\sqrt{\cos \alpha} \approx 0.93.$$

Therefore, this effect is negligible. It caused also increase of the spectral lines width. Suppose that Rowland circle intersects the middle of the CCD chip. Then the distance d of the borders of the CCD from the Rowland circle is

$$d = \sin \alpha d_{CCD}/2 \approx 2 \text{ mm}$$

¹Signal Noise Ratio

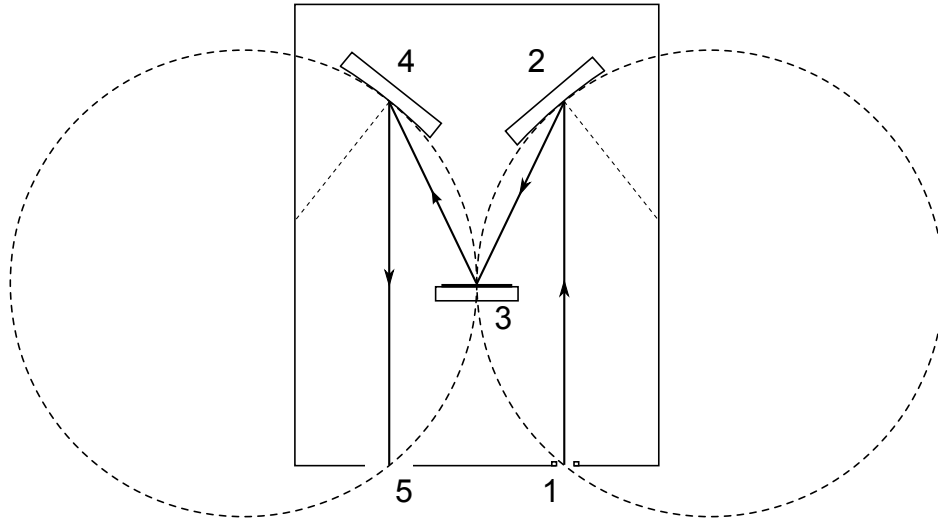


Figure 1.1: The configuration of the high dispersion spectrometer, 1 - input variable width slit, 2,4 - diffraction gratings, 3 - plane mirror, 5 - output focal plane

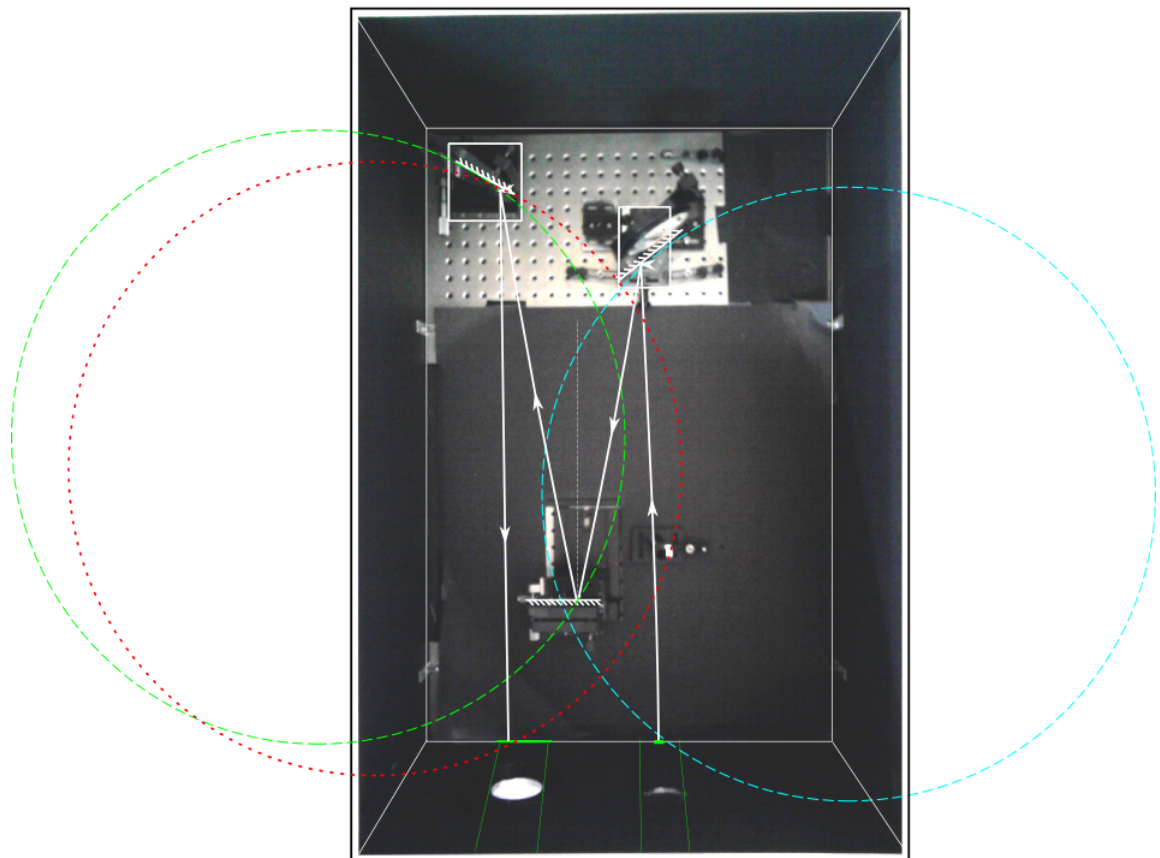


Figure 1.2: A photography of the actual configuration of the spectrometer and the expected positions of the Rowland circles

where $d_{CCD} = 8$ mm is size of the CCD. The FWHM² of the broadening function can be estimated

$$\text{FWHM} = \frac{1}{2} \frac{R_{grating}}{L} \frac{d}{d_{px}} \approx 4 \text{ pixels}$$

where $R_{grating}$ is the radius of grating, L is the distance between the grating and the camera and d_{px} is size of the pixel. The FWHM of this way caused broadening function is approximately 4 pixels on CCD. This effect should be small in comparison with 20 pixels FWHM of the measured peaks, because it causes increase of resulting peak FWHM by only 2%. This effect is very small, but measurable. Nevertheless, when the CIII lines are focused on the middle of the CCD chip, this broadening should be neglected.

1.3 Poloidal Observation System

Light from the tokamak was observed through a system of mirrors and lens from the top and the horizontal port. Both of these lines of sight are drawn in Fig. 1.3. But this configuration cannot be used in future because a new CXRS spectrometer will be installed to the horizontal port. Therefore, when the work on NBI will be finished, the light from the tokamak will be collected from the top and the bottom port (Fig. 1.3, red and blue lines). This way, the blue and red Doppler shift can be observed in the same time. In this section the calculations describing the optical configuration of the latter will be presented.

1.3.1 Optical Path

Analysis of the optical path will be a divided in three parts, the optical path from tokamak to the collecting lens, the collecting lens to spectrometer and the spectrometer.

The first quantity that is necessary to calculate, is the light intensity from tokamak to the last optical element – lens L1. Because the used optical path (Fig. 1.3) was very simple; the results can be achieved with high precision just by an analytical approach. The intensity is the same if the optical elements are placed along straight optical axis. Only the effective height h' of the mirrors will be influenced

$$h' = h \cos \alpha$$

The decrease of the intensity by mirror reflection is negligible. Then the radiant flux Φ is given by following formula

$$\Phi = \int_S dS(\mathbf{x}) \int_V dV(\mathbf{y}) \frac{\epsilon(\mathbf{y})}{4\pi \|\mathbf{x} - \mathbf{y}\|^2} \quad (1.3.1)$$

where $\epsilon(\mathbf{y})$ is plasma radiance, S is surface of lens L1 and V is the plasma volume observed from the point \mathbf{x} . Surface S can be described by vector \mathbf{x} in generalized cylindrical coordinates

$$\mathbf{x} = (r_x \cos \alpha_1 \cos \varphi_x, r_x \sin \varphi_x, 0)$$

where α_1 depends on the position of the middle mirror. When the mirror is further from the lens L1 than $\alpha_1 \approx 0$ and when is close enough to the lens, following approximation is valid $\alpha \approx \pi/4$. Denote the distance between the lens L1 and the last mirror M1 as L , then the coordinate \mathbf{y} of the observed point in the plasma can be substituted

²Full Width Half Maximum

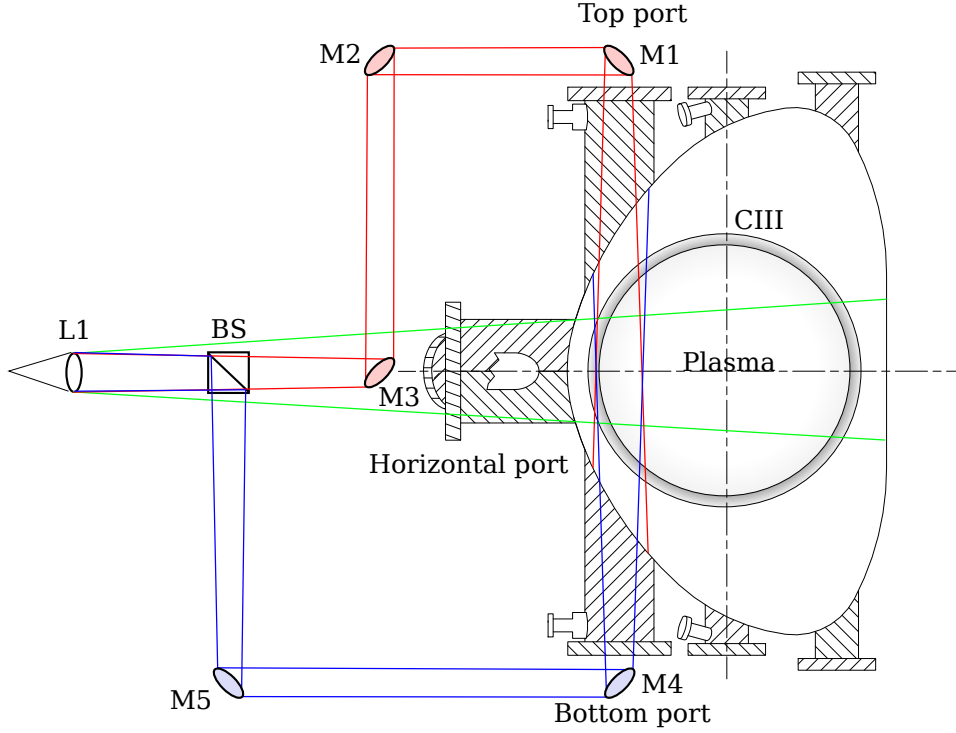


Figure 1.3: The schema of the poloidal cross-section of the tokamak chamber, M1–M5 are mirrors, BS is beam splitter and L1 is the lens focusing light to the spectrometer slit.

$$\mathbf{y} = \mathbf{x} + r_y(\cos \alpha_2 \cos \varphi_y, \sin \varphi_y, 0) + (\mathbf{S}_2 - \mathbf{x}) \frac{z}{L}$$

\mathbf{S}_2 denotes the centre of the mirror M1 and $\alpha_2 = \pi/4$. After these substitutions the formula (1.3.1) can be rewritten as

$$I = \int_0^R dr_x \int_0^{2\pi} \cos \alpha_x d\varphi_x \int_{-\infty}^{\infty} dz \int_0^{r_{max}} r_y dr_y \int_0^{2\pi} \cos \alpha_y d\varphi_y \frac{1}{4\pi z^2} \epsilon(\mathbf{y}(r_y, \varphi_y, \mathbf{x}))$$

r_{max} is defined as $r_{max} = R_2 z/L$. Other calculations cannot be done without knowledge of the radiance $\epsilon(\mathbf{y})$. But rough estimation can be done. Suppose that the emissivity is constant $\epsilon(\mathbf{y}) = \epsilon_0$ for $z \in (L, L + 2a)$, a is tokamak radius, and everywhere else is zero. The light intensity is consequently

$$I = \frac{\epsilon_0}{4\pi} \frac{1}{L^2} \cos \alpha_1 \cos \alpha_2 \pi R_1^2 \pi R_2^2 2a = I_0 \Omega S = I_0 G \quad (1.3.2)$$

where radiant intensity I_0 is defined as $I_0 = 2a\epsilon/4\pi$, $S = \pi R_1^2 \cos \alpha_1$ and $\Omega = \pi R_2^2 \cos \alpha_2/L^2$. Etendue G is defined as ΩS . The radius of the lens L1 is denoted R_1 and the radius of the first mirror is R_2 . The radiant flux Φ can be increased by increasing of mirrors radius R_1 and R_2 . On the other hand, it causes broadening of the observed spectral lines by Doppler shift because of toroidal velocity v_ϕ (more in the Section 3.3).

1.3.2 The Radiant Flux Incoming to the Spectrometer

Now, the calculation of the image projected by the input lens L1 can be processed. The thin lens equation was used. Denote the focal length of the lens f , object distance from the lens z , image distance z' , perpendicular distance from the optical axis of the object r and the image r' . Suppose that the object is small, axially symmetrical and distanced from the lens. This condition is fulfilled in the light path. The properties of the lens, but also other more complicate optical systems, can be described in the first order by affine map (linear map and the shift).

$$\begin{pmatrix} z' \\ r' \end{pmatrix} = F(z, r) \approx F'(z_0, 0) \begin{pmatrix} z - z_0 \\ b \end{pmatrix} + \begin{pmatrix} \frac{z_0 f}{z_0 - f} \\ 0 \end{pmatrix} \quad (1.3.3)$$

where $F'(z_0, 0)$ is the derivation of the map F at the middle of the observed object z_0 . Derivation F' is given by following formula

$$F = \frac{f}{(z_0 - f)^2} \begin{pmatrix} f & 0 \\ 0 & z_0 - f \end{pmatrix} \equiv \begin{pmatrix} \alpha & 0 \\ 0 & \beta \end{pmatrix}$$

where $\alpha = \beta^2$ denotes longitudinal magnification and β is perpendicular magnification. Also other optical elements can be chained just by compounding from these affine maps, but it is necessary to realize, that the etendue of the whole system is equal to the etendue of the narrowest part. Other dimension must be introduced when the system is not symmetrical around the optical axis.

The following problem, which can be analytically calculated, is the irradiance I incidence on the plane perpendicular to the optical axis. Suppose that the lens L1 is uniformly illuminated. The light from each point in the plasma forms a cone with vertex in the image plane. The irradiance can be calculated by integration if this cone over the image of the plasma radiance $\epsilon'(r, z)$ obtained from formula (1.3.3) as

$$I(x, y) = \int_{-\infty}^{\infty} \left(\epsilon'(\tilde{x}, \tilde{y}, z) * \frac{S_{R_z}(\tilde{x}, \tilde{y})}{\pi R_z^2(z)} \right) (x, y) dz \quad (1.3.4a)$$

$$I(r) = \int_{-\infty}^{\infty} dz \int_0^{R_z} \frac{\rho d\rho}{\pi R_z^2} \int_{-\pi}^{\pi} d\varphi \epsilon' \left(\sqrt{r^2 + \rho^2 - 2\rho r \cos \varphi}, z \right) \quad (1.3.4b)$$

where S_{R_z} is indicator function of the circle with radius R_z , s is distance of the slit from len L1, $R_z \equiv |z - s|R/s$ is radius of the cone at position z and R is radius of the lens. The analytical evaluation of the integral (1.3.4b) is complicate even for the most simple shape of the image ϵ' . However, it is possible to make estimation. It is possible to find r_{max} so that for $r > r_{max}$ is $I(r)$ in the eq. (1.3.4b) zero

$$r_{max} = \alpha a R / s.$$

The radiant flux incoming through the slit Φ_i with width w can be estimated as

$$\Phi_i = r_{max} w I \frac{R^2}{r_{max}^2}$$

where I is radiant intensity from the formula (1.3.2).

The final step of this calculation should be the estimation of the throughput of the spectrometer. However, the spectrometer is very sensitive device whose properties are strongly dependent on the precise configuration. Therefore, neglecting of these unknown properties of the spectrometer could cause significant error. Much easier and also more accurate is to measure the properties of the spectrometer experimentally after the final adjustment.

Chapter 2

Signal Processing

The main aim of this chapter is to describe processing of the light signal and effects influencing the signal, in particular different types of noise, quantum efficiency, amplifiers and limited A/D converter sensitivity. And also find the relation between noise and signal for possible settings of the camera. The knowledge of the noise expectable in our diagnostics is necessary to estimate the most advantageous setup.

2.1 Improving of SNR

The driven force behind all low light applications is to increase the Signal-to-Noise Ratio (SNR), defined as

$$\text{SNR} = \frac{\text{Signal}}{\text{Overall Noise}}$$

The SNR can be improved in two ways, by improving signal or reducing noise. The signal can be improved by improving of throughput of optical system. Noise can be reduced for example by cooling of camera or by slower readout speed. Therefore, in this section the main source of noise in the camera will be investigated.

2.1.1 Shot noise

The shot noise arises if the number of the incident photons is low enough to give rise to detectable statistical fluctuations in the measurement. The signal is characterized by the Poisson distribution. Therefore, if only the shot noise is present, the resulting SNR is

$$\text{SNR} = \frac{N}{\sqrt{N}} = \sqrt{N}$$

where N is the number of the counted signals. This noise cannot be suppressed, because the amplification makes no difference. Therefore, the SNR can be improved only by increasing the amount of light caught in the device. It is necessary to realize a trivial idea, that if the other source of noise are negligible, then $4\times$ shorten exposition time causes only halving of the SNR. On the other hand, the exposition must be increased $4\times$ to double SNR.

2.1.2 Dark current

Even, if no light falls on the CCD detector, a weak signal can be measured. It is caused by non-zero temperature of the CCD and consequently spontaneous creating of electron hole pairs. So called dark current is created because of the constant rate of the generated electron-hole pairs, and due to electric fields on a CCD. This current is usually measured in units [electrons/pixel/sec]. The minimal achievable dark current in our camera Andor DU-897E cooled at -100°C is $0.000305\text{ e}^-/\text{px}/\text{s}$ [10]. Dependence of the dark current on temperature is plotted in Fig. 2.1

The number of generated electrons per unit of time is the stochastic process with the Poisson distribution. This noise is added to the shot noise. An easily provable property of Poisson distribution is, that sum of Poisson distribution with parameters λ_i is also Poisson distribution with parameter $\lambda = \sum_i \lambda_i$. Consequently, the dark current causes offset of the observed signal and also increases noise. SNR after including of dark current i_{DC} is given by following formula

$$\text{SNR} = \frac{N}{\sqrt{N + i_{DC}t_{exp}}}$$

where N is number of photoelectrons and t_{exp} is exposure time.

Influence of dark current can be reduced by improving of cooling and shortening expositions. However, for very short expositions, i.e. in our experiment, the dark current is negligible.

2.1.3 Readout Noise

In many instances readout noise can be considered as lowest limit of CCD noise, because dark current can be eliminated by extensive cooling and shorter exposures. This noise do not depend on level of signal, it depends only on the readout speed. Exact values of this noise are measured in Performance Sheet of our Andor iXon^{EM} camera [10]. The probability distribution of this noise signal can be considered as Gaussian $\mathcal{N}(0, \sigma_R^2)$. If the signal intensity is sufficiently high, the Poisson distribution of the signal converges to the Gaussian distribution [12], it can be proved from central limit theorem. The variance of the resulting signal is sum of the signal variance and the variance σ_R^2 of the readout noise. The mean value remains unaffected. SNR, after inclusion of the readout noise, is given by following formula

$$\text{SNR} = \frac{N}{\sqrt{N + i_{DC}t_{exp} + \sigma_R^2}}$$

An internal part of the readout circuit in the used camera is also a preamplifier. The preamplifier amplifies signal G_p times and thus relatively reduce effect of the readout noise to σ_R/G_p . On the other hand, the preamplifier is also a source of noise. Therefore, the readout noise is usually measured for certain setting of preamplifier, it means that gain and noise preamplifier are already included in this value.

The next problem is a A/D convertor that converts charge (photoelectrons) to counts. The convertor has limited sensitivity and thus one e^- is not equal to one count read, it is

only proportional

$$An_c = n_{e^-}$$

where n_{e^-} is number of input electrons, n_c is number of measured count and A [e^-/count] is a proportional constant. The gain G_p is usually included in the constant A , thus the sensitivity can be improved by preamplifier although the real sensitivity of A/D convertor remains unchanged and depends only on the readout speed.

The preamplifier and the limited sensitivity of A/D convertor cause that number of counts measured by camera does not have the Poisson distribution, because even if other sources of noise are negligible, the number of the counts is

$$n_c = \frac{G_p}{AG_p} n_{e^-} = \frac{1}{A} n_{e^-}$$

and the noise

$$\sigma_c^2 = \left(\frac{G_p}{AG_p} \right)^2 n_{e^-} = \frac{1}{A} n_c \neq n_c$$

However the final SNR remains unaffected

$$\text{SNR} = \frac{n_c}{\sigma_c} = \frac{\frac{1}{A} n_{e^-}}{\sqrt{\left(\frac{1}{A}\right)^2 n_{e^-}}} = \sqrt{n_{e^-}}$$

The readout noise can be eliminated by electron multiplication. On the other hand in Section 2.1.5 is detailed discussion about multiplication noise. And the conclusion is that if the square of readout noise is lower than net signal, the electron multiplication cause grown of overall noise.

2.1.4 Quantum Efficiency

Quantum Efficiency (QE) is a quantity defined as the percentage probability that the photon incident the surface of CCD will produce a electron–hole pair. Because the sensitivity of the CCD depends on the wavelength of the photon, also QE is a function of the photon energy. For example in Fig. 2.2 is plotted QE of the Andor DU-897E camera and at the frequency of our interest 460 nm is $\text{QE} = 82\%$. QE influences the noise in two ways. Firstly, it decreases the signal and the second effect is increase of relative influence caused by other sources of noise. The resulting SNR is

$$\text{SNR} = \frac{\text{QE}/100 n}{\sqrt{\text{QE}/100 n + \sigma_{other}^2}} \quad (2.1.1)$$

where σ_{other}^2 includes variances of the signal caused by the other sources of noise. Even if $n \gg \sigma_{other}^2$ the SNR is still decreased by the factor $\sqrt{\text{QE}/100} = 0.91$.

2.1.5 Electron Multiplicative Noise

Electron Multiplication (EM) is based on a cascade of amplification of the signal similar to the avalanche photodiode. EM is therefore stochastic process and thus the gain is not

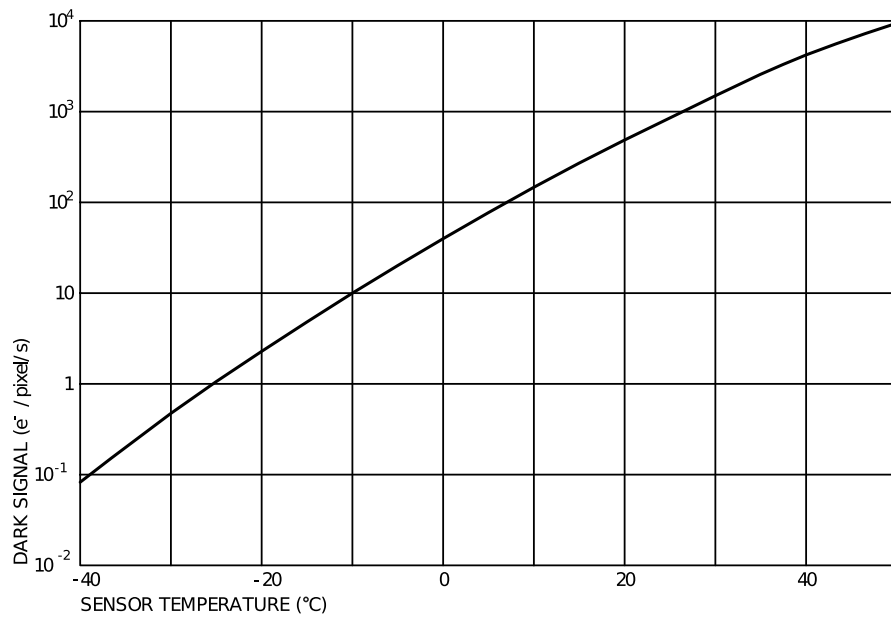


Figure 2.1: A typical variation of the dark current dependent on the temperature for the camera Andor DU-897E [11]

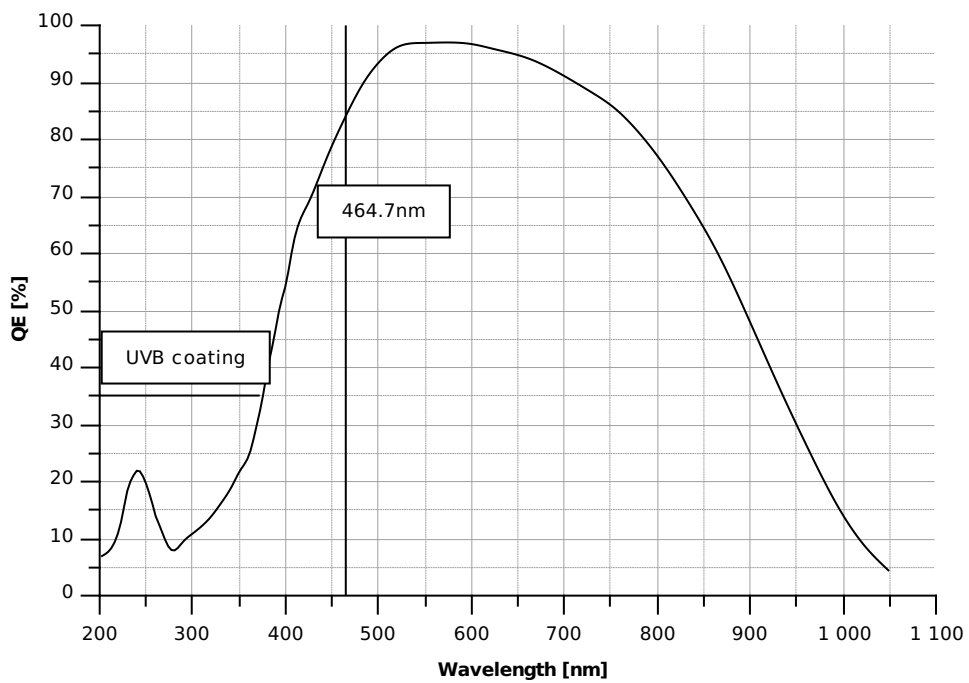


Figure 2.2: QE of the camera Andor DU-897E with standard back illuminated (BV) EMCCD [13]

constant. Variation of gain causes additional noise.

The basic principle of the EMCCD (electron multiplication CCD) is similar to the common CCD, but the main difference is that before the electrons are moved from the readout register to the A/D convertor, they pass through a multiplication register. A schema of this process is in Fig. 2.3. At each stage of this register, electrons are accelerated by an electric field to a potential well. The depth of the well is set sufficiently high in order to electrons can undergo impact ionization processes. Although the probability of this impact ionization is very low (gain ≈ 1.01), the number of stages N can be high enough to achieve the total gain $G_{EM} = g^N \lesssim 1000$.

A method for obtaining an analytical expression of noise increase caused by amplification is shown here. First of all let's consider a single multiplication stage. Number n and m are the mean numbers of the input and the output electrons, σ_n^2 and σ_m^2 are the variances of these random variables. Let's suppose that p is probability of the impact ionization thus creation of a new electron is a Bernoulli process with probability p . Therefore, the number of additional electrons is a random variable with the Binomial distribution and the mean number of the additionally generated electrons is $n_{add} = m - n = np$ and the variance can be expressed as

$$\sigma_{add}^2 = np(1 - p)$$

Consequently, the variance of m is given by the following formula

$$\sigma_m^2 = g^2 \sigma_n^2 + np(1 - p)$$

Under the assumption that the number of the incoming photons n has the Poisson distribution, then the variance σ_n^2 is equal to n and variance after arbitrary number of stages N can be obtained by iterative application of the previous formula

$$\sigma_{out}^2 = \sigma_{in}^2 (p + 1)^{N-1} (2(1 + p)^N + p - 1) = \sigma_{in}^2 G_{EM} \left(\frac{2G_{EM} + p - 1}{p + 1} \right) \approx \sigma_{in}^2 2G_{EM}^2$$

the last approximation is valid only for total gain $G_{EM} \gtrsim 10$.

An experimental verification of this formula is in the article [14]. Also a more accurate formula can be obtained [15], but the accuracy of the previous formula is sufficient for our purposes. Now, the total SNR of the gained signal can be calculated

$$\text{SNR} = \frac{G_{EM} \cdot \frac{QE}{100} n}{\sqrt{2G_{EM}^2 \left(\frac{QE}{100} n + i_{DC} t_{exp} \right) + \sigma_R^2}} \quad (2.1.2a)$$

$$= \sqrt{\frac{QE}{2 \cdot 100}} \sqrt{n} \left(1 + \frac{i_{DC} t_{exp}}{2 \frac{QE}{100} n} + \frac{\sigma_R^2}{2G_{EM}^2 \frac{QE}{100} n} \right)^{-\frac{1}{2}} \quad (2.1.2b)$$

The gain G_{EM} can be chosen sufficiently high to eliminate the readout noise and increase SNR. On the other hand, even if the contribution from the dark current is negligible, the EM noise causes effect equivalent to halving of the quantum efficiency (formula 2.1.2b).

Other common sources of noise, i.e. clock induced charge are negligible in our experiment.

2.1.6 HXR noise

Most of the spectra acquired during plasma discharges in the tokamak included spike noise, example is in Fig. 2.4. The most probable explanation is following; hard x-rays (HXR) photons, caused by runaways or plasma wall interaction (PWI), pass through the tokamak wall and some were captured by the CCD device. The camera was placed about a two meters from the tokamak wall. Capturing of the HXR photon by certain pixel during exposure time is random process with Poisson distribution and the capture rate was usually usually much lower than one photon per pixel.

For understanding the properties of this noise is very important to deal with its physical cause. Energetic photons incident the silicon substrate of CCD and cause huge number of electron-hole pairs because of the avalanche effect. When the whole energy of photon is absorbed, the number of photoelectrons is proportional to the photon energy. However, the used CCD for visible light diagnostics is not thick enough to absorb all energy of the HXR photon. Consequently, significant variation in the number of produced photoelectrons per one HXR photon was observed (Fig. 2.4).

Another unpleasant issue of this noise was in some cases observed significant correlation in noise between neighboring pixels (Fig. 2.4 160–180 pixel). There exist two possible explanations. The first is that photon incident a CCD obliquely and influenced more pixels along its track. The second explanation is based on expectation, that number of generated photoelectrons was so huge, that arise overflow from potential well of the influenced pixel to surrounding pixels.

In the future experiments this noise can be removed by lead shielding of camera. But in already measured data, this noise has been removed numerically. Detailed description of the algorithm for data filtering is described in the section about data analysis 2.2.

2.1.7 Background Light

The light from the tokamak plasma is conducted through an open system of mirrors and lens and thus the day light or light from other sources enters to the spectrometer and also the stray light inside the spectrometer cause additional noise. It causes increase of noise and increase of data offset in similar way as dark current. Therefore, the light intensity I [photons/s/pixel] can be included to “effective dark current” i'_{DC}

$$i'_{DC} = i_{DC} + \frac{QE}{100}I$$

This light can be slightly eliminated by turning off the lights in tokamak hall.

2.1.8 SNR – Conclusion

The final and most general formula to determine the number of counts n_c is

$$n_c = \frac{G_{EM}}{A} \left(\frac{QE}{100}n + i'_{DC}t_{exp} \right) + BG_p G_{EM} \quad (2.1.3)$$

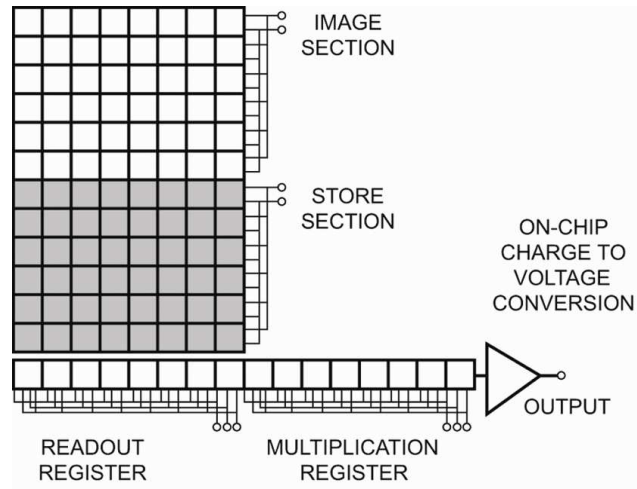


Figure 2.3: A schema of the EMCCD array

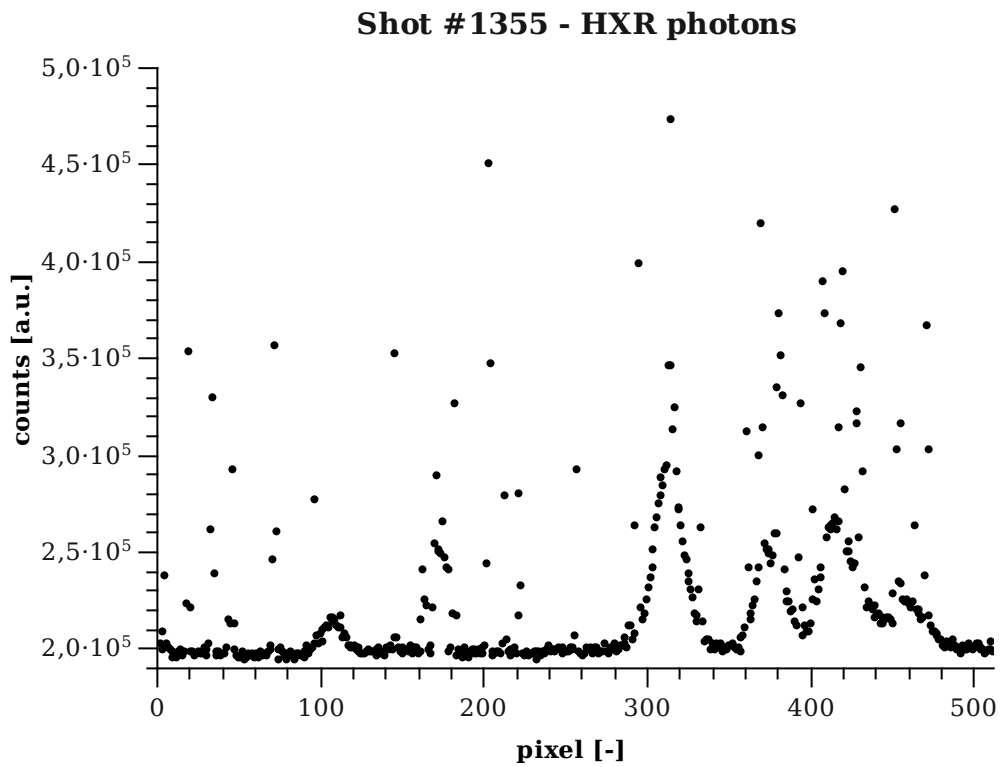


Figure 2.4: An example of a spectrum of shot #1355 containing HXR noise.

where n is number of incident photons per pixel, A is sensitivity (preamplifier gain is already included in this constant) and B is baseline offset, which is added to signal to ensure, that the number of counts is always positive. The offset B is approximately to 400 counts at -50°C in our camera. The offset depends on actual settings and conditions of the camera. The general formula for variation of number of counts takes following form

$$\begin{aligned}\sigma_c &= \frac{\sqrt{2}G_{EM}}{A} \sqrt{\left(\frac{QE}{100} n + i'_{DC} t_{exp}\right) + \frac{\sigma_R^2}{2G_{EM}^2}} \\ &= \sqrt{\frac{2G_{EM}}{A}} \sqrt{(n_c - B A G_p) + \frac{A\sigma_R^2}{2G_{EM}}}\end{aligned}\quad (2.1.4)$$

If is the electron multiplication turned off, the gain factor $\sqrt{2}G_{EM}$ is replaced by one. It is obvious, that even if is the number of captured photon very high, and the variance of number of counts is only proportional to counts, not equal. This formula is in agreement with measured noise better than 4%.

Now, it is possible to estimate the most appropriate setting for the camera. The minimal SNR is limited by requirements for sufficiently precise fitting of the spectra. The noise at the top of the peaks should be lower than 5%, consequently the SNR should be greater than 20.

- The shot noise is limited by number of photons. The QE within spectral region of our spectrometer is 82% (Fig. 2.2), hence at least 400 photons are necessary to achieve $\text{SNR} > 20$. Light radiant flux incident on the CCD is limited by plasma conditions and position. The required amount of light was integrated for plasma discharge length ~ 5 ms.
- The dark current at temperature -55°C is approximately $0.01e^-/\text{px}/\text{s}$ and by the exposure 50 ms, vertical binning of CCD over 512 px, the mean value of noise is $0.3e^-$ and hence it is negligible. Background and stray light depends on final configuration of the spectrometer and the light in the tokamak hall.
- The readout noise depends only on the readout speed and the preamplifier gain. The root mean square (RMS) of the noise for 1 MHz readout speed and maximal preamplifier gain is $8.6e^-$. This readout speed should be sufficient for our experiment, 512 vertically binned pixel can be readouted in only 1.45 ms. The influence of readout noise can be reduced by the EM amplification, but from equations (2.1.1) and (2.1.2b) it is evident, that if the number of photon is greater than square of the readout noise, the higher SNR can be reached without EM. The same conclusion can be obtained from Fig. 2.5.

Finally, the optimal mode is 5 ms exposure, 1 MHz readout speed and EM switched off. However, exposures shorter than 5 ms should be also possible. For example in shot #1613 observed from top port, with duration 5.4 ms, the SNR was 140 and attainable SNR for 1.5 ms exposure, $200\mu\text{m}$ width slit and conventional amplifier is 90 and it is still perfect result.

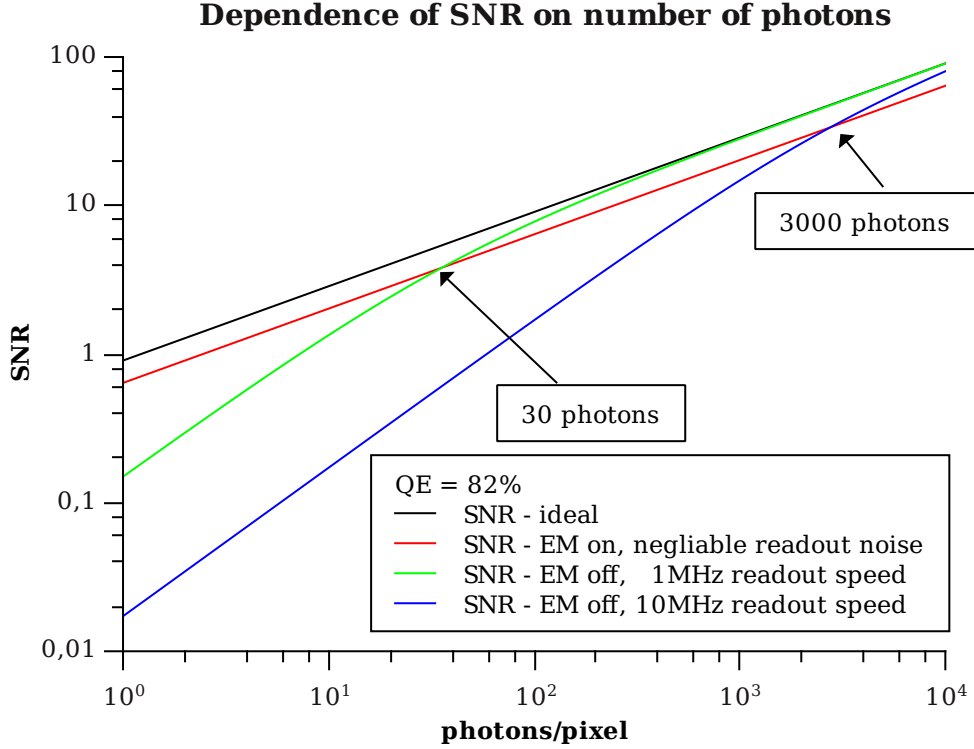


Figure 2.5: Comparison of SNR for different camera configuration.

2.2 Data Filtering

After the extraction of data from the camera and before fitting, numerical filters must be applied. Firstly, se necessary to remove the HXR noise (subsection 2.1.6), because huge amount of outliers affect even the robust reweighted least square method [16], which has been used for the data fitting.

The pixels influenced by the HXR photons must by indentified and removed, because they completely lost the information about the previous number of captured photons. An algorithm (filter) for their identifying and removing is introduced in this section.

First of all, suppose that the mean value μ_i of the observed spectrum of i -th pixel uninfluenced by the HXR photons is known. The random variables X_i describing the signal of the i -th pixel (without the HXR noise) has approximately the Gaussian distribution with mean $EX_i = \mu_i$ and variance $\sigma_i^2 = E(X_i - \mu_i)^2 = C\mu_i$, where C is constant depending on setting of camera (eq. (2.1.4)). The random variable determined by previous formula has the normal distribution $X_i = \mathcal{N}(\mu_i, C\mu_i)$ and the most of the outliers can be easily identified because their value does not lie in 95% confidence interval. Another possibility is to apply the iterative procedure called Grubbs' test [17] to identify outliers.

The previous described methods suffer from an important disadvantage; the exact profile of the spectrum μ_i is unknown. Therefore was used the sequence of filters. The goal of the individual filters is to find the best possible approximation of the real profile of spectrum influenced by HXR photons and remove only the most suspicious points for example by Grubbs test or just by trimming.

2.2.1 Median Filter

The easiest way, how can be the profile of the spectrum from the data extracted is by moving average, because average is maximal likelihood estimator of the Gaussian distributed data. But the mean is not a robust statistical estimator. Thus a moving median instead of the mean was applied on the data.

This median filter can reconstructs almost perfectly monotone functions, but it causes cutting of the peak and thus the length of the moving window should be as short as possible. On the other hand if more than half of the pixels in moving window are influenced by HRX noise, median loses the position of the correct data. Example of this failure is in Fig. 2.6 between 160–180 pixels. When more than 50% of all pixels is damaged (so called *break point* of this robust statistics), this filter is unusable for arbitrary length of window.

2.2.2 Low-pass Filter

The second filter is based on cutting off the high frequencies by the Fourier transformation. An advantage of this approach is perfect fitting of the peaks on the contrary to the median. Disadvantages are lower resistance against correlated noise, sensitivity to very far outliers and problem with fitting of the base of sharp Gaussians, because cutting of HF part of the Fourier cause “rippling” of the of Fourier curve. This filter is therefore usable only for less noisy spectra (Fig. 2.6).

The most effective solution is removing the most distanced outliers by median filter and then applying more precise filtering by the low pass Fourier filter.

2.2.3 A Priori Knowledge Base Filter

Previous approach is unproductive for the damaged spectrum, where most of the pixels were damaged and another algorithm had to be used. In Fig. 2.6 is shown that values of the damaged pixels are always higher than the correct ones. Therefore, one of the solutions is fitting the noisy spectrum by the model function $f(x, \theta_j)$, where θ_j are parameters of this function, but instead of classical NLLSQ must be used asymmetrical weighting function $w(x)$, for example

$$w(x) = \begin{cases} \frac{(y_i - f(x_i, \theta_j))^2}{\sigma_j^2} & \text{if } y_i - f(x_i, \theta_j) \geq 0 \\ \tanh\left(\frac{(y_i - f(x_i, \theta_j))^2}{\sigma_j^2}\right) & \text{if } y_i - f(x_i, \theta_j) < 0 \end{cases}$$

After the fitting the data can be statistically filtered or trimmed in the same way as in the previous filters. The most successful was combination of all these filters. The example of an obtained filtered spectrum is a noisy shot #1609 in Fig.2.7

2.3 Model Function

It can be proved that if the examined data have Gaussian distribution, then the maximum likelihood estimator (MLE) of the parameters of the model function can be obtained by

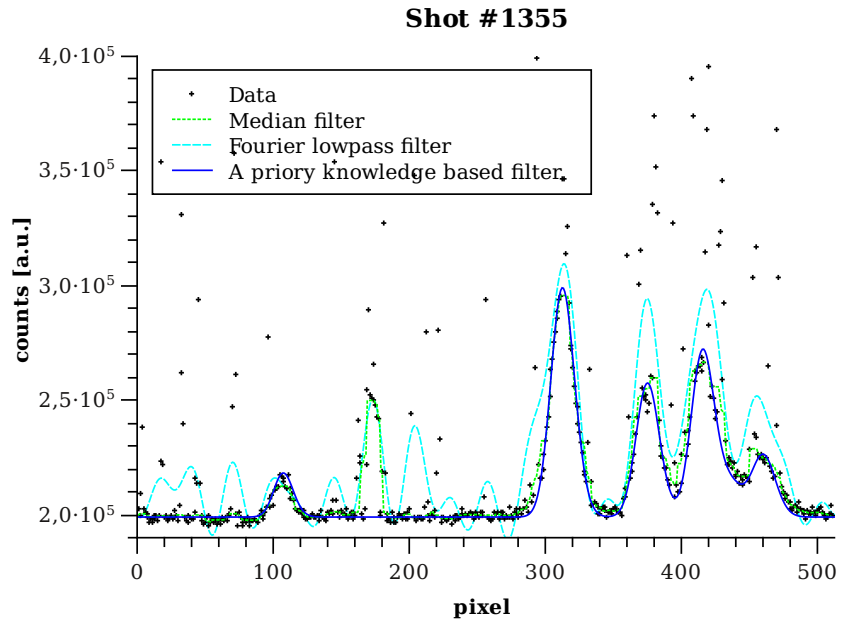


Figure 2.6: An example of different filters applied on the original spectrum

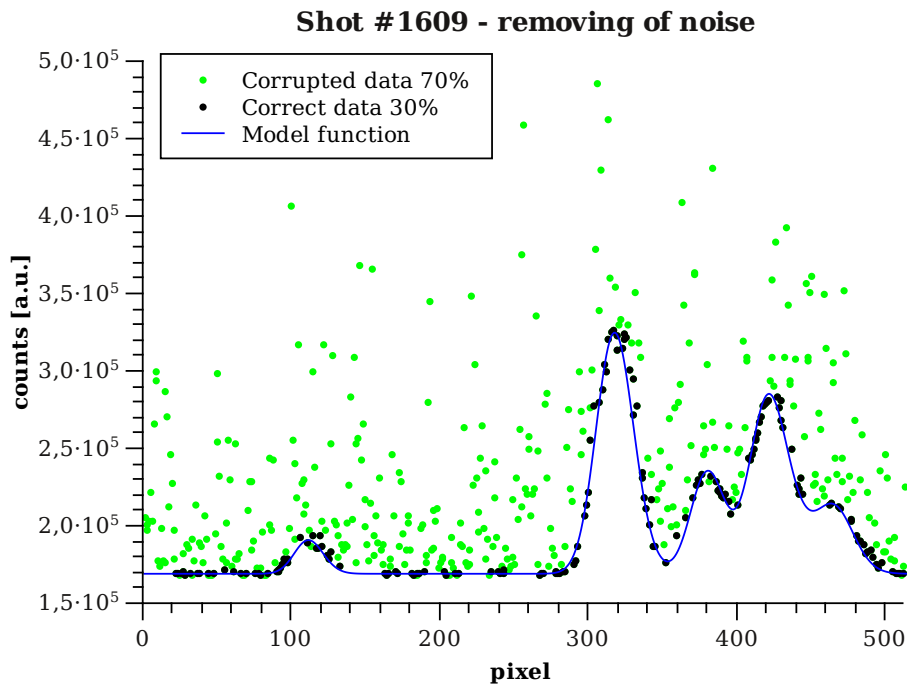


Figure 2.7: Identified and removed noise by a priori knowledge based filter in noisy spectrum of shot #1609

weighted nonlinear least square (WNLLSQ) method.

The simplest model function and also the first tested was mixture of Gaussians plus a constant offset. This model composed from 5 Gaussians depends on 16 parameters. However, this model was proved to be unusable, because of obviously non-Gaussian profile of peaks (Fig. 2.8), the reason will be discussed in the Section 3.5. The most of the peaks were characterized by considerable skewness. Consequently, a more complicated model based on the skew Gaussian functions [18] was applied. The comparison of the fit between the skew Gaussian curve and the ordinary Gaussian curve is in Fig. 2.8. The formula of skew Gaussian function is following

$$f(x) = \frac{a}{\sqrt{2\pi w^2}} \exp\left(-\frac{(x - \xi)^2}{2w^2}\right) \left(1 + \operatorname{erf}\left(\alpha \frac{x - \xi}{\sqrt{2}w}\right)\right) \quad (2.3.1)$$

parameter α influences the skewness of this distribution. Basic properties of the previous function are summarized in following table

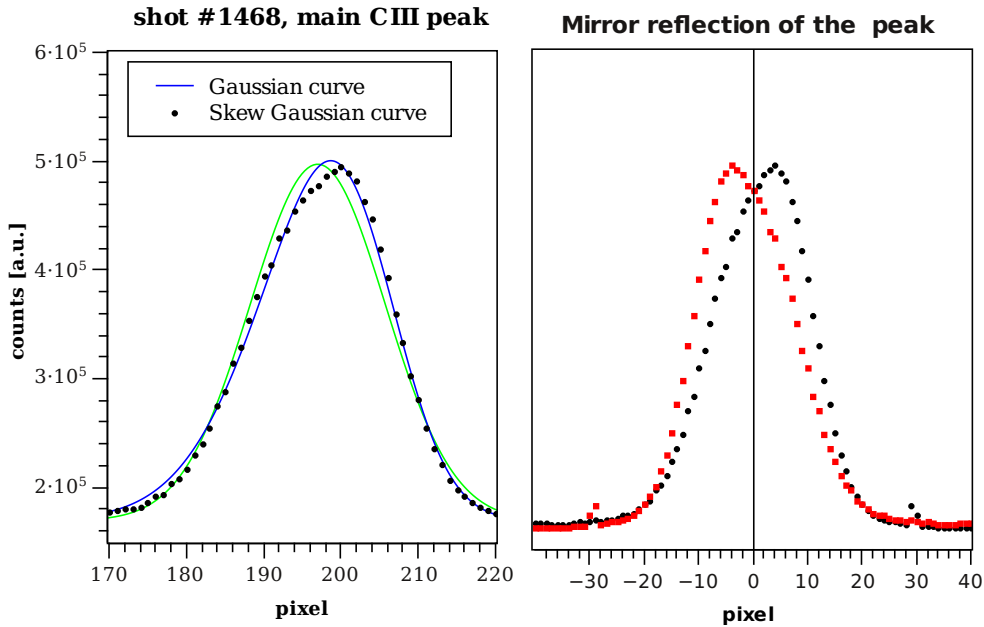


Figure 2.8: The main CIII peak fitted by ordinary and skew Gaussian and the mirror reflection of the original data where is considerable skewness clearly visible.

$$\text{mean} \quad \mu = \xi + w\delta\sqrt{2/\pi} \text{ where } \delta = \frac{\alpha}{\sqrt{1 + \alpha^2}}$$

$$\text{variance} \quad \sigma^2 = w^2 (1 - 2\delta^2/\pi)$$

$$\text{skewness} \quad s = \frac{4 - \pi}{2} \frac{(\delta\sqrt{2\pi})^3}{(1 - 2\delta^2/\pi)^{3/2}}$$

$$\text{area} \quad A = a$$

An obvious disadvantage of this model function is increased number of parameters. It is necessary to fit 5 peaks with 21 parameters. In addition, the difference between the

skewness and temperature determined from CIII peak 4650Å and from other peaks in the same spectrum was statistically significant. It was partially caused by a hidden OII peak between the lower CIII peaks (Fig. 2.9) and consequently the appropriate model function should consist of mixture of six skew Gaussians depending on 25 parameters and the most of them is ill conditioned.

In order to achieve as much as possible stable model, an apriori knowledge about the spectrum must be applied to minimize the number of the free parameters and to improve the statistical precision of the remaining parameters. The first investigated parameters will be the positions of the peaks. These six parameters can be calculated from the dispersion of the spectrometer, tabularized wavelengths of spectral lines and the only one fitted parameter is the shift. In the case of significant rotation shear at the edge of plasma, the Doppler shift of CIII and OII lines can be slightly different and in this case two shift parameters $\Delta x_C, \Delta x_O$ are required.

The six parameters determining the skewness can be replaced by one without notable increase of the residuum. The temperature of CIII ions and therefore the Doppler broadening of the all CIII lines should be the same and also the width of OII lines should be the same. Therefore the six parameters determining width of peaks can be calculated from OII temperature (T_O), CIII temperature (T_C) and from the instrumental broadening. But this simple assumption was shown as not valid (section 3.4.2), the most probable causes are discussed in chapter 3. At least the ratios of the peaks widths can be considered to be constant within confidence intervals.

The last six parameters determine area of the peaks. It should be possible to calculate from theory [19] the ratios between the areas of CIII triplet. This problem is discussed in detail in the next chapter, but the result is that relative intensities of the CIII and OII remain constant and are unaffected by plasma conditions at least within the statistical significance. Therefore, the 6 parameters determining the area under the peaks can be replaced by two parameters, the absolute intensity A_C and A_O of one CIII and one OII peak.

Finally, all the 26 parameters can be estimated from 5–6 parameters: $T_C, (T_O), \Delta x_C, A_C, A_O, B$. The skewness s depends probably only on position of camera and configuration of spectrometer (will be discussed in chapter 3). Therefore it can be considered of being constant. Example of spectrum fitted only by these 5 parameters is in Fig.2.9

But still, the model function can be expected as the mean of real profile only if the variance in signal sufficiently high, because with increasing accuracy of the response the inaccuracy of our theoretical model function model appears. Than the conditions under that the NLLSQ was derived are not valid and measured values of response are not located in expected confidence interval. This problem will be verified in detail by numerical simulation in the next chapter.

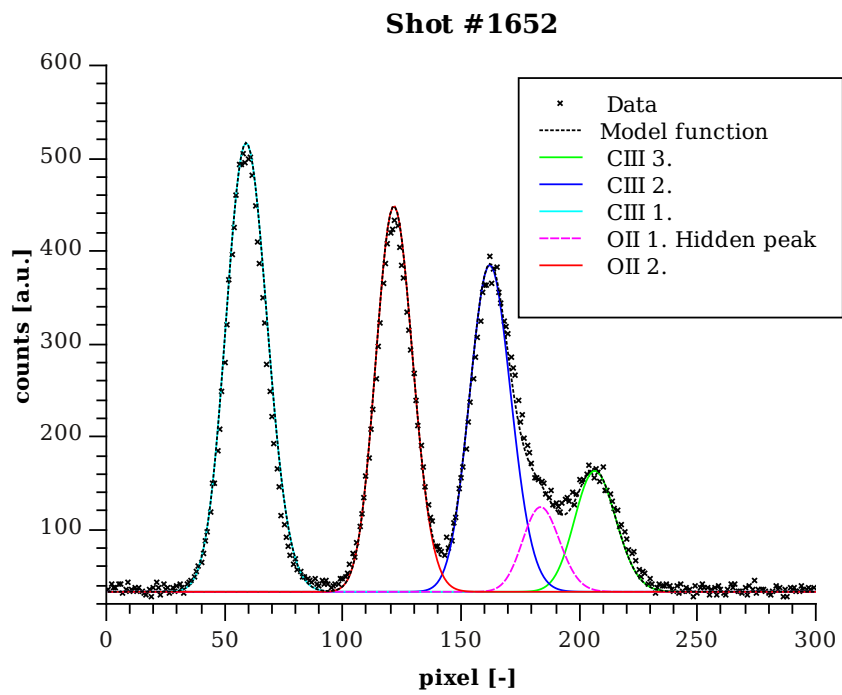


Figure 2.9: The spectrum with extraordinary intense OII lines and the peak of OII hidden between two CIII peaks. The spectrum was fitted by 5-parameters model function (Sec. 2.3)

Chapter 3

Results and Discussion

The results extracted from 51 spectra obtained between the shots 1349 to 1703 measured on tokamak COMPASS are discussed in this chapter. Example of the spectrum with described peaks is in figure 3.1. The spectrometer was set in a temporary setup and therefore the results were not the technical limits of this device. All spectra obtained during these first measurements are processed and analyzed and improvements of configurations are suggested based on these results.

The main aim of this spectrometer is measuring of the poloidal rotation velocity and ion temperature on the plasma edge. But also other plasma properties can be measured. For example, the relative concentration of impurities ions OII and CIII and line integrated concentrations of these ions can be estimated.

The last important note, all of the results and error bars in graphs are calculated with 95% confidence intervals.

3.1 Spectrometer

It was necessary to determine basic properties of the spectrometer. But there were two problems. The first, a spectral lamp with the line within the spectral region of the spectrometer was not disposal. And the second, the camera was removed from spectrometer ater the tokamak campaign and therefore even if some spectral calibration lamp would be disposal, it is impossible to set up the spectrometer to the same configuration as were the spectra acquired. Therefore, the only way, how to extract some properties of the previous configuration of spectrometer, is directly from the measured spectra.

3.1.1 Dispersion

The easiest way, how to obtain the dispersion, is directly from fitting of spectra. Ordinary spectral lamps does not have more than one usable line in spectral region of the spectrometer and therefore it is the only precise way to determine dispersion. The dispersion d was determined as

$$d = (27.47 \pm 0.19) \cdot 10^{-3} \text{ \AA/px} = 1.717 \pm 0.011 \text{ \AA/mm}$$

Example of the spectra from shot #1349

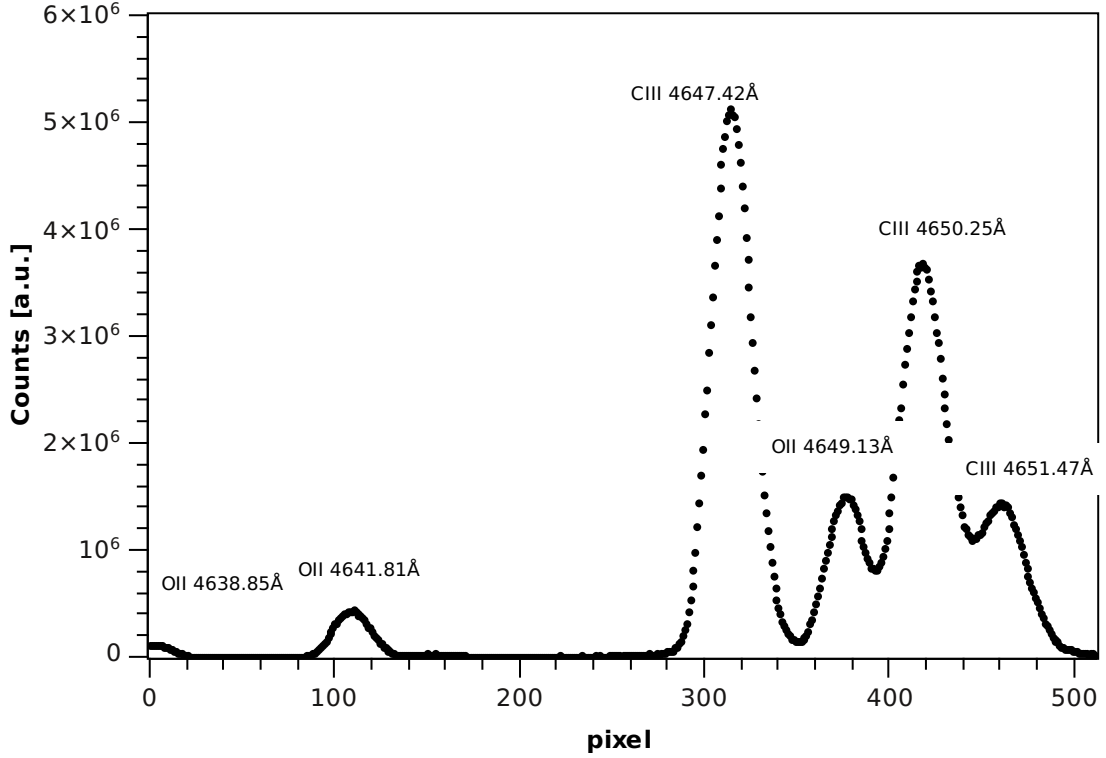


Figure 3.1: Example of observed VIS spectrum

The value measured in Portugal [5] is slightly different $d = 1.65 \text{ \AA/mm}$.

3.2 Instrumental Broadening

The finite slit width, the finite size of diffraction grating and other effects, for example imperfect configuration of spectrometer cause broadening of observed spectral lines. The profile of the observed line ϕ_{out} is therefore given by convolution of the input spectra ϕ_{in} and an instrumental broadening function f_i

$$\phi_{out}(y) = (\phi_{in} * f_i)(y) = \int \phi_{in}(y-x)f_i(x)dx \quad (3.2.1)$$

If the input profile ϕ_{in} is an ideally narrow spectral line, mathematically describable by Dirac δ -function, the profile ϕ_{out} is the same as broadening function $f_i(x)$. Instead of ideally narrow spectral line can be certainly use real spectral line with FWHM significantly less than FWHM of $f_i(x)$. Also for approximately Gaussian broadening function the convolution can be calculated and ϕ_{out} stays Gaussian with FWHM

$$\Delta\lambda_{1/2}^G{}^2 = \Delta\lambda_{1/2}^{G_1}{}^2 + \Delta\lambda_{1/2}^{G_2}{}^2$$

for more complicated instrumental broadening functions, the convolution with the Gaussian can be estimated analytically from the expansion of $f_i(x)$ to the first terms of the ortonormal Hermitian functions [20] or by moment expansion [21]. The FWHM from

profile of the input line can be calculated by “deconvolution”

$$\Delta\lambda_{1/2}^{G_{in}} = \sqrt{\Delta\lambda_{1/2}^{G_{out}^2} - \Delta\lambda_{1/2}^{G_i^2}} \quad (3.2.2)$$

For widely opened slit between 200-400 μm , used in the most of the measurements, is thereby caused broadening the main reason of spectral line broadening of the spectrometer. From simple geometry and schema of spectrometer (Fig. 1.1) can be deduced that the image of slit is projected on the CCD of camera without any significant change of the size and therefore, the observed broadening function f_i caused by slit should be rectangular. The resulting profile f_{out} can be calculated from convolution

$$f_{out}(x) = (f_i * f_{in})(x) = \frac{1}{2}\sqrt{\pi} \left(\text{erf} \left(\frac{w}{2a} - x \right) + \text{erf} \left(\frac{w}{2a} + x \right) \right)$$

where w is width of the slit and a is width of one pixel on CCD. For narrower slit width also the FWHM of resulting profile $\Delta\lambda$ (in pixels) can be estimated from variance of unitary distribution

$$\Delta\lambda^2 = 8 \ln 2 \left(\frac{w^2}{12a^2} \right) + \Delta\lambda_{1/2}^{G^2}$$

constant $c \equiv \sqrt{8 \ln 2 / 12a^2} = 0.042 \text{ px}/\mu\text{m}$ is rough approximation of measured value c' .

$$c' = 0.056 \pm 0.008 \text{ px}/\mu\text{m}$$

The different can be caused by diffraction broadening of the spectrometer or other neglected effects.

3.3 Plasma Rotation

The spectrometer was set to a temporal configuration (Chapter 1), the similar configuration as in Portugal [5] and therefore only rough verification of rotation velocity should be possible. The reference Doppler unshifted spectral lines were observed from equatorial line of sight, perpendicularly to the toroidal and the poloidal rotation of the plasma column. And the shifted lines were observed from the top port at the tangential line of sight (to the plasma shell containing CIII ions) and perpendicular to the toroidal rotation of the plasma. The observed line profile is given by following formula

$$I(\nu) = \frac{1}{4\pi} \int_{t_{exp}} \int_V \phi \left(\nu - \frac{\nu}{c} (\mathbf{v}_{\mathbf{p}} \cdot \mathbf{n}(\mathbf{r}, \mathbf{r}')), T(\mathbf{r}, t) \right) \epsilon(\mathbf{r}, t) d\Omega(\mathbf{r}') dV(\mathbf{r}) dt \quad (3.3.1)$$

where t_{exp} is the exposure time, V is the observed volume of the plasma, $\phi(\nu, T)$ is local Gaussian profile of line, $\mathbf{v}_{\mathbf{p}}$ plasma velocity, $\mathbf{n}(\mathbf{r}, \mathbf{r}')$ unit vector with direction $\mathbf{r} - \mathbf{r}'$, ϵ is radiant flux density and Ω is solid angle. After perfect align of optical path the toroidal velocity v_{ϕ} causes only broadening of spectral lines, because the formula (3.3.1) can be

rewritten as

$$I(\nu, t) \propto \int_V \epsilon(\mathbf{r}, t) \delta \left(\nu - \frac{\nu_0}{c} v_\theta(\mathbf{r}, t) \cos \alpha(\mathbf{r}, \mathbf{r}') \right) * \phi(\nu, T) d\Omega(\mathbf{r}') dV(\mathbf{r}) \quad (3.3.2)$$

$$= \left(\int_{V \cap \{\cos \alpha(\mathbf{r}, \mathbf{r}') = \Delta \nu v_\phi / (\nu c)\}} \epsilon(\mathbf{r}, t) d\Omega(\mathbf{r}') dV(\mathbf{r}) \right) * \phi(\nu, T) \quad (3.3.3)$$

When is the mean value of $\alpha(\mathbf{r}, \mathbf{r}')$ zero, the first integral causes only broadening of the spectral function $\phi(\nu)$. Broadening due to poloidal velocity is an order of magnitude smaller and therefore negligible.

In the first order approximation, the line profile is determined only by

$$\phi \left(\nu \left(1 - \frac{v_\theta}{c} \right), T \right)$$

The measurement procedure consisted of two steps. In the first step, a few unshifted spectra from the equatorial line of sight were measured and then the optical path was changed and the shifted spectra from tangential line of sight were achieved. The measurement is based on the assumption of shot reproducibility. But this condition was not fulfilled on the tokamak COMPASS. Therefore, the plasma discharges collected by this spectrometer cannot be considered as identical. Therefore most similar shots acquired during one day without any intervention. The most similar are shots 1513, 1515, 1519, 1522, 1523, collected during one day in equatorial line of sight. The basic properties of these shots are in Tab. 3.1. During this day the configuration of spectrometer was not changed and therefore most of the results in this Section will be discussed on these similar shots.

shot number	shot duration [ms]	max I_p [kA]	$\langle n_e \rangle [10^{19} \text{m}^{-3}]$
1513	14.3	16.5	0.66
1515	17.49	20	0.6
1519	7.22	26	2.05
1522	5.64	26.0	0.97
1523	5.79	26.4	1.08

Table 3.1: Basic properties of the most important investigated shots.

The mean values of the shifts and the corresponding poloidal velocities v_{pol} are in table 3.2. It is obvious that this shift cannot be caused only by Doppler shift, because in this case the shift from horizontal to top port and back from top to horizontal should be the same. Therefore, the poloidal rotation from the observed spectra is improvable.

Change of position	between shots #	observed shift [px]	poloidal velocity
H→T	1556→1569	$\Delta = -22.3$	$v_{pol} = -38 \text{ km s}^{-1}$
T→H	1574→1578	$\Delta = -1.9$	$v_{pol} = -3.3 \text{ km s}^{-1}$
H→T	1578→1604	$\Delta = 14.0$	$v_{pol} = 24.1 \text{ km s}^{-1}$

Table 3.2: The shifts of the spectra caused by a change of the optical path from the top (T) to horizontal (H) port and back.

It can be explained in three different ways. The change of the optical path caused that the collected light from plasma come through different part of the input slit of the spectrometer. But the change of the spectra positions should be less than instrumental broadening,

approximately 4 pixels. The second explanation is based also on the change of optical path. If the line of sight is not perpendicular to the toroidal rotation, also this Doppler shift could be measured. One degree deviation from perpendicular direction cause for toroidal rotation approximately 100 km s^{-1} the shift of spectra 1 pixel.

But these two explanations still cannot explain the measured shifts (tab. 3.2). However the change of optical path the a fine adjustment of the mirrors along optical path was performed. During this adjustment the spectrometer box was opened and even a careful manipulation could cause the slight displacement of the optical elements inside of the spectrometer.

In Fig. 3.2 is the slight shift of the spectra observed from equatorial line of sight. This shift is definitely not caused by an imprecise fitting of the spectra, because the shift is clearly visible from the raw data. Consequently, it was caused by projection of toroidal rotation to the line of sight or by temperature expansion of spectrometer or the whole device also with camera during the day. The coefficient of liner temperature expansion of ordinary steel is $10^{-5} \text{ }^\circ\text{C}^{-1}$ and for aluminum $2 \cdot 10^{-5} \text{ }^\circ\text{C}^{-1}$. Therefore, only a change of temperature about $1 \text{ }^\circ\text{C}$ could cause the shift of spectra $10\text{--}20 \text{ } \mu\text{m}$ and shift in camera $0.5\text{--}1.5$ pixel.

These problems should be solved by measuring of the shifted and the reference line at the same time and by precise alignment of the optical path. Two different approaches can be chosen. The first method is based on observing the reference spectral line and determining the shift from the difference between reference line and the CIII line. As a reference line can be used a copper hollow cathode lamp with a bright spectral line 4651 \AA or a considerable weaker line of a Ne lamp at 4645.42 \AA [22]. Also a iron hollow cathode lamp should have a line within the spectral region of the spectrometer. The position of the reference line can be measured before or after the plasma discharge.

The error of poloidal velocity σ_v measured this way can be estimated:

$$\sigma_v = v \sqrt{\left(\frac{\sigma_d}{d}\right)^2 + \frac{\sigma_r^2 + \sigma_s^2}{(\Delta)^2}} \approx v \frac{\sigma_s}{|\Delta|} \approx \frac{c}{\nu} \sigma_s = 0.2 - 0.4 \text{ km s}^{-1} \quad (3.3.4)$$

where d is dispersion, Δ is Doppler shift, σ_s and σ_r are error estimates of spectrum position and position of reference line, c is speed of light and ν is observed wavelength. The expected precision σ_s based on measured spectra is $0.1\text{--}0.2$ pixel, σ_r/σ_s and should σ_d/d be negligible.

The second method called differential Doppler spectroscopy [23] is based on observation of the plasma from two opposite line of sight. The blue shift will occur in the first and the red shift in the second. Both of these spectra are observed at the same time on different halves of the CCD chip. The precision of this method can be estimated from following formula

$$\sigma_v = v \sqrt{\left(\frac{\sigma_d}{d}\right)^2 + \frac{\sigma_{s1}^2 + \sigma_{s2}^2}{(2\Delta)^2}} \approx \frac{v}{\sqrt{2}} \frac{\sigma_s}{|\Delta|} \approx \frac{c}{\nu} \frac{\sigma_s}{\sqrt{2}} \quad (3.3.5)$$

The achievable precision should be therefore $\sqrt{2} \times$ higher than in previous method, but the expected arrangement of the experiment (Chapter 1) causes decrease of signal at least $2 \times$ in beamsplitter. SNR and statistical error of fitted spectra are inversive proportional

(simulation in Fig. 3.3). Therefore the precision will be equal or worse than with the reference line. Advantages of the differential Doppler spectroscopy is simple detection of the projection of the toroidal rotation velocity to the shift.

The precision of the velocity measurement is also influenced by the slit width. Too narrow slit causes decrease of SNR and therefore decrease of precision, on the other hand, increase of slit width causes increase of instrumental broadening. The results from a numerical simulation are in Fig. 3.4. In conclusion the most advantageous slit width is between 150–250 μm .

3.4 Ion temperature

The other important edge plasma parameter measurable by the spectrometer is ion temperature. The thermal motion of particles causes so called Doppler broadening of spectral lines. The shape of the Doppler broadened lines $f(\lambda_D)$, can be easily calculated

$$f(\lambda_D)d\lambda_D = \tilde{f}(v)\frac{d\lambda_D}{dv}dv = \tilde{f}(v)\frac{c}{\lambda_0}d\lambda_D$$

where λ_D is Doppler shifted wavelength, and v is corresponding velocity. For the Maxwell distribution is line shape Gaussian

$$f(\lambda_D) = \tilde{f}\left(\lambda_D\frac{c}{\lambda_0}\right)\frac{c}{\lambda_0} = \sqrt{\frac{mc^2}{2\pi kT\lambda_0^2}}\exp\left(-\frac{mc^2\lambda_D}{2kT\lambda_0^2}\right)$$

and FWHM is

$$\lambda_D = 2.35\lambda_0\sqrt{\frac{T[eV]}{m[eV]}} \quad (3.4.1)$$

The Doppler broadening of impurities lines was measured, hence the temperature of majority particles can be different from this temperature. Due to collisions the thermal equilibrium between different species occurs with collision frequency [24]

$$\nu_e \sim 10^{-12}\frac{\sqrt{\mu_1}n_1Z_1^2Z_2^2}{\mu_2(T_1/e)^{3/2}}$$

μ represents the nucleon number of the particles. The relaxation time is approximately 0.1 ms and therefore the temperature equilibrium between carbon and oxygen impurities and hydrogen ions can be assumed in flattop if NBI is not working.

3.4.1 Line Integrated Temperature

The plasma radiation is observed through line of sight (chord) passing plasma with different conditions. The profile of spectral line $\phi(\nu)$ is then obtained by ignoring the shift in the formula (3.3.1)

$$\phi(\nu) \propto \int_{\Delta t} dt \int_V dV \phi_l(\nu, T(\mathbf{r}, t))X(T(\mathbf{r}, t))n_i(\mathbf{r}, t)n_e(\mathbf{r}, t) \quad (3.4.2)$$

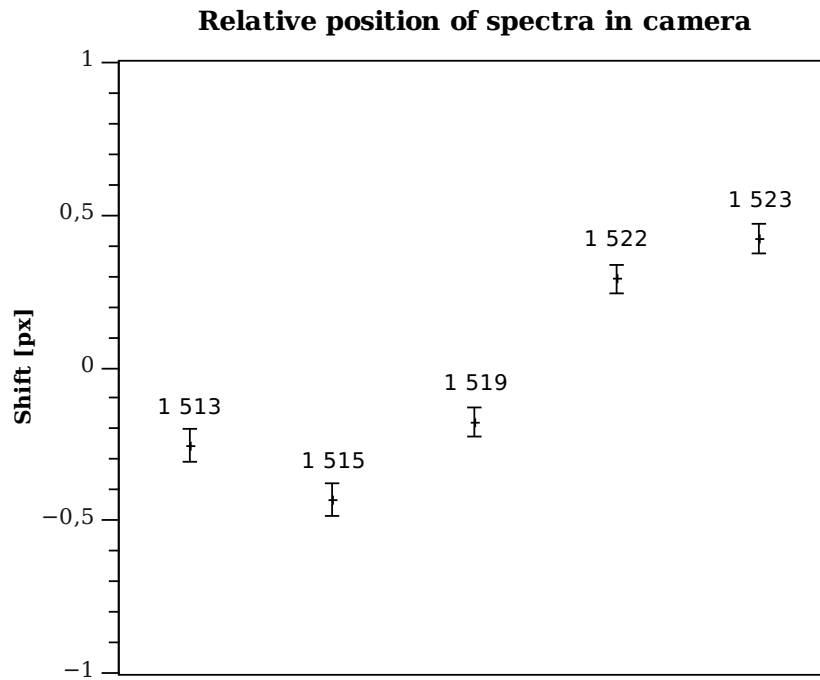


Figure 3.2: The shift of profiles of spectral lines observed from equatorial line of sight.

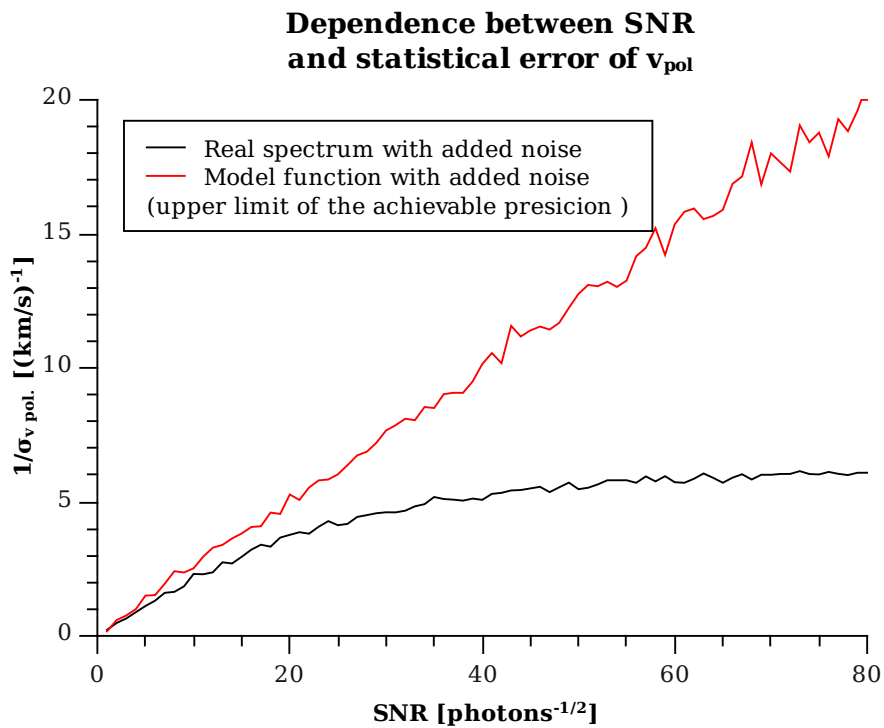


Figure 3.3: Statistical error of v_{pol} simulated by fitting of real noiseless spectrum (shot #1519) and model function, both with additional Poisson noise, by 5-parameters model function (sec. 2.3).

Dependence between slit width and statistical error of v_{pol}

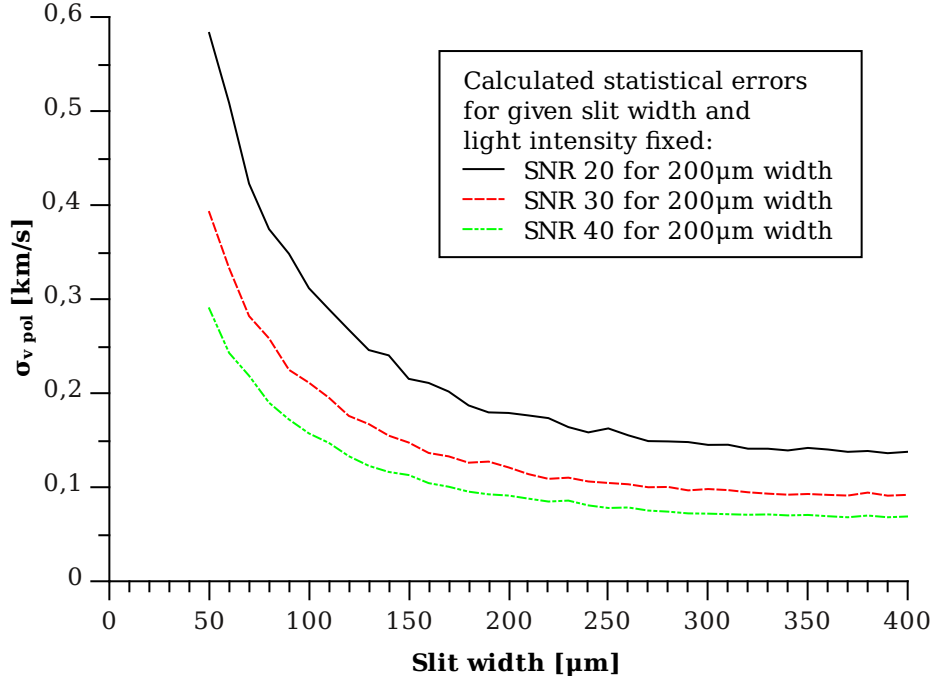


Figure 3.4: A numerical simulation of the dependence between statistical error of v_{pol} and slit width

where $\phi_l(\nu, T)$ local profile of the Doppler s line depending only on the local temperature profile $T(r, t)$, $X(T)$ is excitation rate coefficient, $n_i(\mathbf{r}, t)$ is density of the observed ions (CIII or OII), n_e is electron density and the integration is taken over observed volume of the plasma V during exposure time Δt .

The problem of line integrated temperature measurement can be unexpectedly complicated. Lets suppose that the steady state high temperature plasma is observed, this condition can be fulfilled in confinement volume of plasma. Then the density of CIII or OII ions $f(\mathbf{r})$ nonzero only on thin hollow shell on the edge of the plasma and depends only on temperature profile $T(\mathbf{r})$ [25]. The position of this shell can be estimated from transport codes [26] if the ion temperature profile at the edge is known or can be measured by spatial resolved spectroscopy [22]. But the profile of ion temperature at the edge is not measured by other diagnostic and this spectrometer probably cannot be improved to measure with spatial resolution over more chords.

A few approximations can be done in the formula (3.4.2). Suppose the that exposure time is so short that time dependant functions in equation (3.4.2) can be considered as constant during Δt . If the electron density n_e is low enough, the coronal equilibrium can be approximately expected. The impurity ion density n_i can be expressed from the concentration c and electron density n_e

$$n_i(\mathbf{r}, t) = c(T(\mathbf{r}, t)) n_e(\mathbf{r}, t)$$

concentration is in coronal equilibrium only a function of the temperature [25] and due to significant gradient of the temperature on the plasma edge, the concentration is consider-

able higher than zero only at few centimeters wide shell [22] behind the LCFS. Suppose that in the region, where $c(T(\mathbf{r}, t))$ is nonzero, the temperature and electron density can be approximated by their first two terms of Taylor expansion calculated at the point of maximum concentration multiplied by excitation rate coefficient $X(T_0)c(T_0)$. Suppose that line of sight is tangential to the shell of nonzero concentration c (for perpendicular direction will be following conditions fulfilled even better), and the chord is wider than the shell. Then the integration over observed plasma volume in eqv. (3.4.2) can be replaced by integration along radial coordinate

$$\int_V dV f(\mathbf{r})c(\mathbf{r}) = l\Delta\varphi \int_{\Delta r} dr f(r)c(r)$$

Δr is the region where $c(r)$ is nonzero, l is “mean” length and $\Delta\varphi$ is the toroidal width of the chord independent of plasma properties.

$$\begin{aligned} \phi(\nu) &\propto \int_{\Delta t} dt \int_V dV \phi_l(\nu, T(\mathbf{r}, t))X(T(\mathbf{r}, t))n_i(\mathbf{r}, t)n_e(\mathbf{r}, t) \\ &\approx l\Delta\varphi\Delta t \int_{\Delta r} dr \phi_l(\nu, T(r, t))X(T(r, t))c(T(r, t))n_e^2(r, t) \end{aligned} \quad (3.4.3)$$

Now, can be applied the previous assumptions and used only linear Taylor expansion of n_e^2 and T in r .

$$\begin{aligned} \phi(\nu) &\propto \int_{\Delta r} dr \phi_l(\nu, T(r, t))X(T(r, t))c(T(r, t)) \left(n_e^2(r_0, t) + \left. \frac{dn_e^2}{dr} \right|_{r_0} (r - r_0) \right) \\ &\approx n_e^2(r_0, t) \left(\left. \frac{dT}{dr} \right|_{r_0} \right)^{-1} \int_{\Delta T} dT \phi_l(\nu, T)X(T)c(T) \\ &+ \left. \frac{dn_e^2}{dr} \right|_{r_0} \left(\left. \frac{dT}{dr} \right|_{r_0} \right)^{-2} \int_{\Delta T} dT \phi_l(\nu, T)X(T)c(T)(T - T_0) \\ &= n_e^2(r_0, t) \left(\left. \frac{dT}{dr} \right|_{r_0} \right)^{-1} A(\nu) + \left. \frac{dn_e^2}{dr} \right|_{r_0} \left(\left. \frac{dT}{dr} \right|_{r_0} \right)^{-2} B(\nu) \end{aligned} \quad (3.4.4)$$

$$\propto A(\nu) + \frac{1}{n_e^2} \frac{dn_e^2}{dr} \left(\left. \frac{dT}{dr} \right|_{r_0} \right)^{-1} B(\nu) \quad (3.4.5)$$

Functions $A(\nu)$, $B(\nu)$ are independent of the plasma properties and therefore in this approximation of the observed line profile is explicitly independent of the ion temperature. It is caused especially by the assumption that light from impurities is emitted from narrow shell and observed by wider line of sight.

Therefore if these previously mentioned conditions are fulfilled, line integrated temperatures are independent of the local temperature.

3.4.2 Line Integrated Ion Temperature – Results

The FWHM of the two CIII peaks was influenced by the hidden OII peak. Therefore, the height of this peak was precisely determined from fitting of all spectra with extraordinary

intense OII peaks, and than the height of the hidden OII peak was fixed to be proportional to the rest of OII peaks. This way allowed to completely remove the influence of the hidden peak. The spectra was then fitted by mixture of Gaussian without any a priory knowledge, except the wavelengths (Sec. 2.3). An example of the estimated temperatures from shots 1513–1523 is in Fig. 3.5.

In particular, difference in temperatures for different spectral lines is interesting. It is expectable that temperature of OII ions should be lower than CIII because of different ionization temperatures. More interesting is difference between both OII peaks, the FWHM of these OII lines was about 50% different and it is definitely much more than could be explained by an uncertainty of the fit. Also for CIII lines can be observed the same effect. This effect can be observed for all shots in the database not only in these selected shots. The most simple explanation was an inaccurate spectrometer align and configuration. The CCD chip of camera probably does not lie on the Rowland circle of the spectrometer (Chapter. 1), but one side of CCD is closer than another.

Also other mechanisms affecting width of line are present in the plasma. The most of them are negligible compared to the Doppler broadening or cannot be neither confirmed nor disproved by our experiment, for example fluctuation broadening [25].

Additional broadening can be caused by toroidal rotation of plasma (formula (3.3.1)). The broadening depends on the final configuration of the optical path, but it was approximately 1 pixel. Exact value of the broadening can be calculated from the toroidal velocity that must be measured by new CXRS spectrometer.

In clear and noiseless spectra another broadening was observed (Fig. 3.6). This broadening is not Gaussian, because otherwise the resulting profile obtained by convolution would be also Gaussian. It can be caused by the imperfection of the optical gratings or by the plasma itself. The decision can be made on the base of the spectra from the calibration spectral lamp.

The most common non-Gaussian plasma broadening is the Stark broadened, which is approximately Lorentzian, but it can be also asymmetrical for heavier ions [19]. The result from fitting shot #1519 (Fig. 3.6) by Voigt profile¹ is following; the Gaussian shape has FWHM 20.8 pixels and Lorenz has FWHM 1.5 pixels. But the Stark broadening does not influence the temperature, because the FWHM of the Voigt profile is almost the same as FWHM of the original Gaussian profile calculable from formula [27]

$$f_V \approx 0.5346 f_L + \sqrt{0.2166 f_L^2 + f_G^2} = 21.6 \text{ pixel}$$

However, Stark broadening should be negligible in the tokamak plasma [25].

3.5 Asymmetrical Profile of the Spectral Lines

In the previous Section 2.3 a problem with the skewness of Gaussian peaks was mentioned. The measured skewness fitted by model function without any a priory knowledge (Sec. 2.3) with removed hidden OII peak (Sec. 3.4.2) is in Fig. 3.7. These spectra were observed from equatorial line of sight. The skewness of different peaks is significantly different. High uncertainty of one OII peak is caused by its low intensity.

¹convolution of Lorentz and Gaussian profile

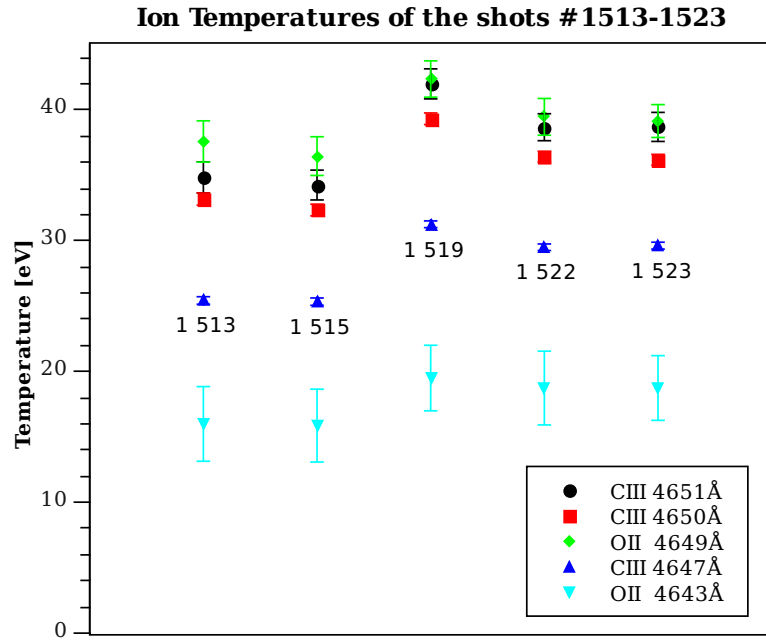


Figure 3.5: Ion temperatures evaluated from formula (3.4.1), the influence of the hidden peak (Sec. 2.3) was removed.

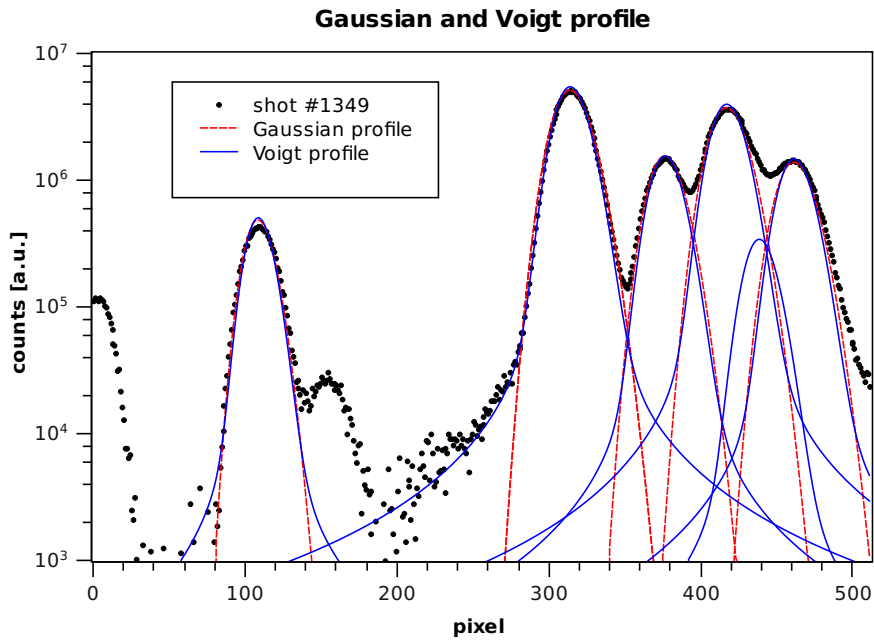


Figure 3.6: Non-Gaussian broadening of the base of the peaks

More explanations of this skewness exist. It could be caused by plasma properties; this would explain the changes of skewness in different shots in Fig. 3.7. On the other hand, decrease of the skewness could be caused by an increase of line width due to increase of temperature (Fig. 3.5) or increase of slit width. The increase of width causes smooth out of the line.

The skewness can be also caused because integration time Δt of camera was longer than discharges and therefore the time dependence of the Doppler shift could appear (simplification of formula(3.3.1))

$$\phi(\nu) \propto \int_{\Delta t} \phi \left(\left(1 + \frac{v(t)}{c} \right) \nu \right) I(t) dt$$

The resulting spectral line profile $\phi(\nu)$ is therefore the mean of the Doppler shifted profiles weighted by its intensities $I(t)$. The velocity $v(t)$ can be caused by poloidal rotation velocity in the case of tangential line of sight, but also in the case of imperfect align the toroidal rotation velocity can appear even in equatorial line of sight. However, no significant differences in skewness between equatorial and tangential line of sight have been observed.

Unfortunately, this cannot explain different skewness of different lines. Even other effects that can occur in the plasma as asymmetrical Stark broadening, Zeeman Effect cause the same skewness for all CIII triplet lines. The most probable explanation is again the imperfect configuration of spectrometer, because a convolution with skew instrumental broadening function causes also skewness of the resulting function.

It can be also reason of different skewness of different lines. Also it is possible that the higher broadening of bluer lines (3.5) is closely connected to the observed increase of the skewness of bluer lines. The relation between the changes of the mean skewness of the line profiles and the changes of configuration of spectrometer and camera can be obtained from Fig. 3.8.

3.6 Intensities of the Observed Spectral Lines

The last important property directly measurable from the lines profiles is the lines intensity. An absolute calibration of the spectrometer will be possible after setting the spectrometer to the final configuration (Chapter. 1). Therefore, only relative intensities of spectral lines can be calculated now.

3.6.1 Relative Intensities

The relative intensities of the observed lines in the stationary plasma were measured to be constant, probably independent of the plasma conditions. The relative intensities of the lines in the CIII triplet obtained from all measured shots are in Fig. 3.9 and OII lines are in Fig. 3.10.

The relative intensities of the CIII triplet should be easily computable. The CIII triplet lines are populated from the same level, thus difference in energy should be lower than

0.3%, differences in Einstein coefficients A_{ij} are lower than 0.3% [28]. The only relevant parameter influencing the ratios of the CIII triplet peaks intensities is a degeneration of the upper level. Consequently, the relative intensities of triplet lines should be given only by relations of lines degenerations.

However, the relative intensities are significantly different from the expected values (Fig. 3.9). Some mechanism caused decrease of the more intense lines or decrease of the bluer lines.

In the case, that it is not caused by plasma, it can be caused by the spectrometer, the camera or output glass windows from the tokamak. Significant gradient of transitivity or quantum efficiency could cause decrease of bluer lines. But it can be calculated, that decrease of transitivity or QE must be almost 10% per 1Å and it was not observed. It could be also caused by the significant efficiency gradient of the gratings [6]. Therefore, this property should be verified by high power calibration tungsten lamp during the planned recalibration of the spectrometer.

And the last possibility is that this effect is caused by the plasma. In similar experiment conducted NSTX tokamak [22] was obtained almost perfect agreement between expected and measured relative intensities. On the other hand, in experiment conducted in Portugal [5], with the same spectrometer the relative intensities of distinguishable lines were similar to the values measured on tokamak COMPASS. However the measured intensities of these peaks were significantly influenced by broadening caused probably by MCP (Microchannel plate detector) used in their experiment.

3.6.2 Absolute Intensities

The intensity of the spectral line is determined by integration of formula (3.3.1) over wavelengths. The number of photons coincidental to the input slit of spectrometer can be estimated as (Chapter 1.3)

$$N = \frac{1}{h\nu} \int_V \int_{t_{exp}} \epsilon(\mathbf{r}, t) \frac{\Omega(\mathbf{r})}{4\pi} dV dt$$

The absolute values $\epsilon(\mathbf{r}, t)$ integrated along the line of sight can be then determined from this spectrometer. From the absolute value of $\epsilon(\mathbf{r}, t)$ can be estimated by radiative collisional model FLYCHK [29] the density of the CIII and OII ions and even the concentration of the impurities C and O.

Absolute calibration can be done by calibrated high power light source with known spectral intensity profile from known solid angle. For example calibrated ribbon tungsten lamp can be used.

.

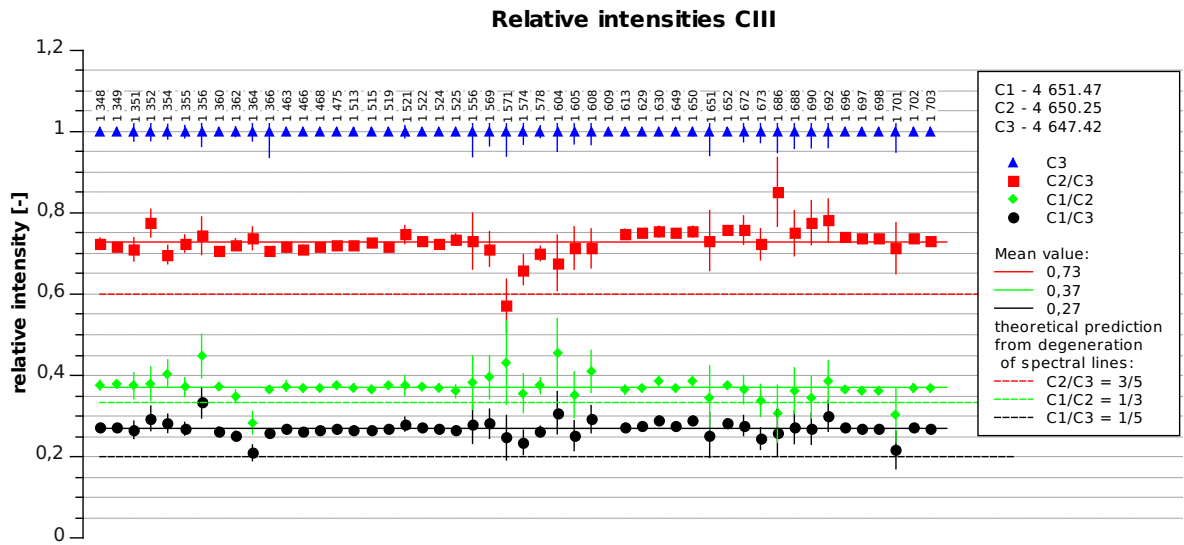


Figure 3.9: Relative intensities of lines of CIII triplet compared with expected values.

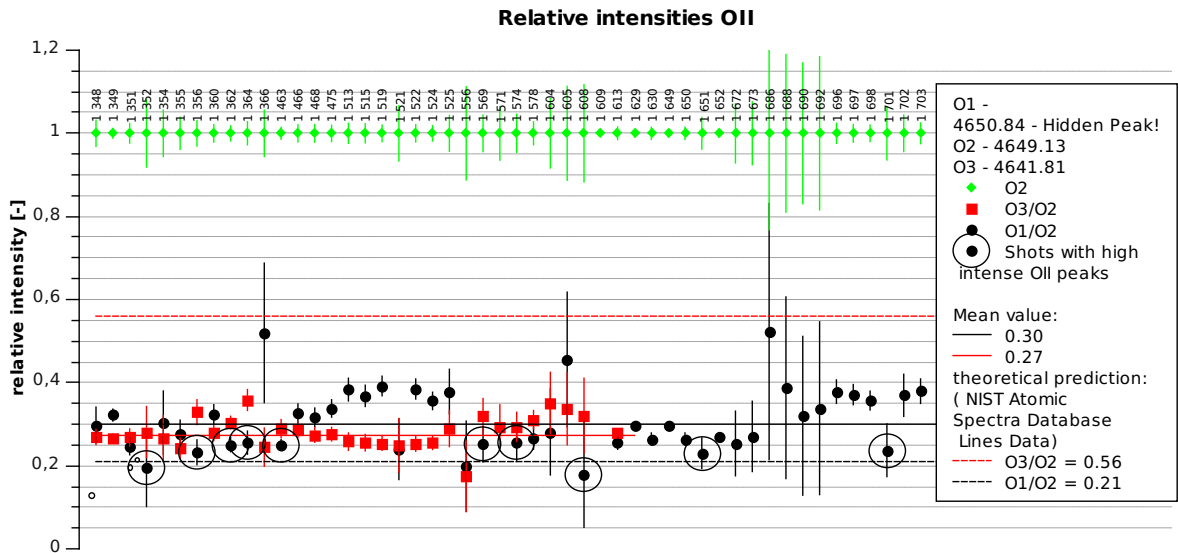


Figure 3.10: Relative intensities of OII spectral lines also with values for hidden peak. The results for relative intensity of hidden peak are the most trusty from the spectra with high intensity of OII lines.

Summary

Significant part of this research work deals with thorough analysis of the method used for the measurements of the plasma poloidal rotation velocity. In the rest of the work, the resulting spectra obtained by high resolution spectrometer were discussed. In the first chapter, the properties of the optical path of the spectrometer were estimated. The most advantageous setting of the used camera was determined in the second chapter. The camera setting is based only on a few shots from the top port of tokamak and therefore the final settings can be slightly different. The last chapter is devoted to interpretation of the measured spectra. The obtained results were discussed in this work and possible explanations were suggested also the procedures to their verification or disproving were found. However, these improvements could not be tested, because the tokamak COMPASS was in service-shutdown during writing of this research work.

Therefore, this work can be continued by implementations of the suggested improvement and finally, by measurement the real poloidal rotation velocity of the plasma.

Bibliography

- [1] F. Wagner. A quarter-century of h-mode studies. *Plasma Physics and Controlled Fusion*, 49:B1, 2007.
- [2] Z. Lin, T.S. Hahm, W.W. Lee, W.M. Tang, and R.B. White. Turbulent transport reduction by zonal flows: Massively parallel simulations. *Science*, 281(5384):1835, 1998.
- [3] Basil. P Duval. Experimental results on intrinsic rotation. 1st EFDA GPM, IPP Garching, May 5-6, 2011.
- [4] P. Mantica. Experimental results for cor momentum transport studies and a comparison with simulation/theory. 1st EFDA GPM, IPP Garching, May 5-6, 2011.
- [5] R.B. Gomes, C.A.F. Varandas, J.A.C. Cabral, E. Sokolova, and S.R. Cortes. High dispersion spectrometer for time resolved Doppler measurements of impurity lines emitted during ISTTOK tokamak discharges. *Review of Scientific Instruments*, 74(3):2071–2074, 2003.
- [6] C.A. Palmer and E.G. Loewen. *Diffraction grating handbook*. Newport Corporation, 2005.
- [7] J.W. Coenen. *The Influence of the Dynamic Ergodic Divertor on the Radial Electric Field at the Tokamak TEXTOR*. Forschungszentrum Julich, 2009.
- [8] H.A. Rowland. LXI. Preliminary notice of the results accomplished in the manufacture and theory of gratings for optical purposes. *Philosophical Magazine Series 5*, 13(84):469–474, 1882.
- [9] A. Sokolova, Elena, Santiago D. Reyes Cortes, and Nelson Mineiro. High-resolution spectrometer for tokamak plasma diagnostics. *Proc. SPIE 3130, 160*, 1997.
- [10] Andor *iXoin^{EM} + Performace Sheet*. Model: DU-897E-CS0-BV .
- [11] e2v technologies. CCD97 Back Illuminated peltier cooled – Datasheet. online, 2004. [cit. 2011].
- [12] G.R. Shorack. *Probability for statisticians*. Springer Verlag, 2000.
- [13] Andor. iXonEM+ 897 (back-illuminated) – specification sheet. online.
- [14] M.S. Robbins and B.J. Hadwen. The noise performance of electron multiplying charge-coupled devices. *Electron Devices, IEEE Transactions on*, 50(5):1227–1232, 2003.

- [15] T. Cajgfinger and B.P. Dirac. Simulations and Localization Accuracy of Image Sensors in their Environment: Theoretical and Monte Carlo Methods.
- [16] W.H. Press, S.A. Teukolsky, W.T. Vetterling, and B.P. Flannery. Numerical recipes 3rd edition: The art of scientific computing. 2007.
- [17] F.E. Grubbs. Procedures for detecting outlying observations in samples. *Technometrics*, 11(1):1–21, 1969.
- [18] A. Azzalini. A class of distributions which includes the normal ones. *Scandinavian journal of statistics*, 12(2):171–178, 1985.
- [19] H.R. Griem. Principles of plasma spectroscopy. *Proceedings of the Physical Society*, 1, 2005.
- [20] C. Hermite. *Sur un nouveau développement en série de fonctions*. Compt. Rend. Acad. Sci.
- [21] A. Papoulis. Systems and transforms with applications in optics. *McGraw-Hill Series in System Science, Malabar: Krieger, 1968*, 1, 1968.
- [22] TM Biewer, RE Bell, R. Feder, DW Johnson, and RW Palladino. Edge rotation and temperature diagnostic on the National Spherical Torus Experiment. *Review of scientific instruments*, 75:650, 2004.
- [23] N.C. Hawkes and N. Peacock. A novel multichord spectrometer for plasma velocity measurements. *Reviews of Plasma Physics*, 63(11):5164, 1992.
- [24] G. Schmidt. Physics of high temperature plasmas. 1979.
- [25] I.H. Hutchinson. *Principles of plasma diagnostics*. Cambridge Univ Pr, 2002.
- [26] Weinzettel. V. *Prostorové a časové chování lehkých nečistot ve vysokoteplotním plazmatu*. PhD thesis, CVUT FJFI, 2004.
- [27] J.J. Olivero and R.L. Longbothum. Empirical fits to the Voigt line width: A brief review. *Journal of Quantitative Spectroscopy and Radiative Transfer*, 17(2):233–236, 1977.
- [28] Yu. Ralchenko, A.E. Kramida, J. Reader, and et al. NIST Atomic Spectra Database (ver. 4.0.1). *National Institute of Standards and Technology, Gaithersburg, MD*, <http://physics.nist.gov/asd>, [2011, March 27].
- [29] H.K. Chung, MH Chen, WL Morgan, Y. Ralchenko, and RW Lee. Flychk: Generalized population kinetics and spectral model for rapid spectroscopic analysis for all elements. *High energy density physics*, 1(1):3–12, 2005.